Material Characterization of Electrodeposited Copper-Nickel Nanolaminated Alloy by SEM, EDS, and XRD

Irene Cheryl Wang

A thesis
submitted in partial fulfillment of the
requirements for the degree of

Master of Science in Materials Science and Engineering

University of Washington
2012

Committee:
Brian Flinn
Lucien Brush
Jihui Yang

Program Authorized to Offer Degree:
Materials Science & Engineering

University of Washington

Abstract

Material Characterization of Electrodeposited Copper-Nickel Nanolaminated Alloy by SEM, EDS, and XRD

Irene Cheryl Wang

Chair of the Supervisory Committee:
Associate Professor Brian Flinn
Materials Science & Engineering

Electrodeposited nanolaminated copper-nickel alloys (Cu-Ni) exhibit excellent mechanical properties due to their modulated structure and nanocrystalline microstructure. X-ray diffraction, scanning electron microscopy, and energy dispersive X-ray spectroscopy were used to characterize the composition, grain size, phases, and laminate structure of a nanolaminated deposit to explore structure-process-property relationships. The processing method of interest was pulse current electrodeposition of Cu-Ni a rotating disk electrode (RDE) with increased rotation speed during deposition of Cu-rich layers. Although copper content was enhanced in this way, it also caused macroscopic swirls in the deposit's surface, which were reflected microstructurally as Cu-rich streaks, non-planar layers, and other inhomogeneous morphology in the nanolaminate coating. Bulk composition of the nanolaminate was calculated from XRD spectra as being over 67wt%Ni overall, with over 91wt% Ni in Ni-rich layers and over 43wt% Ni in Cu-rich layers. EDS data of the same deposit differed significantly from these values, suggesting an overall composition closer to 55 wt% Ni, with a Ni-rich layer composition of 81 wt% Ni and 8.4 wt% Ni in the Cu-rich layers. Grain sizes of 15.8-22.3 nm were calculated for the nanolaminated deposit compared to 13-19 nm grains in a monolithic Ni-rich deposit of Cu-Ni.

Table of Contents

List of Figures

List of Tables

Glossary

nanolaminated alloy – an alloy which consists of alternating layers of metallic compositions with nanocrystalline grains and nanoscale layer thicknesses

monolithic – consisting of a single, uniform composition; a monolithic *Ni-rich* coating in this thesis is one that is fully composed of an unlaminated Ni-rich copper-nickel alloy

electrodeposition; *electroplating* – a process where a pulsed or direct electric current is applied to an anode and cathodic substrate submerged in an electrolytic plating bath solution to deposit a material (usually metallic) or materials onto the cathode from solution

Acknowledgements

I would like to thank Dana Rosenbladt, Tamon Page, and Hanson Fong for their assistance with SEM training and data collection. Dana deserves extra thanks for sharing her expansive general insight throughout this project on everything from sample polishing techniques to thesis-writing tips! I am also thankful of Brian Flinn for his much-appreciated support and knowledgeable guidance. Thank you to Jihui Yang and Lucien Brush for their exceptionally kind addition to my defense committee! I would also like to thank Tuesday Kuykendall for refreshing my knowledge of X-ray diffraction and for her assistance training me to use the department XRD and Jade.

1. Introduction

1.1. Background Information

Nanocrystalline materials in general, with grain sizes smaller than 100 nm, tend to exhibit lower elastic moduli, higher hardness, increased ductility and fatigue resistance, and higher tensile strength compared to conventional polycrystalline, coarse-grained materials [1, 2]. An increase in tensile strength is expected from the Hall-Petch relationship, where fine grain sizes correlate to a high density of grain boundaries, which impede dislocation movement during plastic deformation [3]. Further increasing grain boundary density in metallic alloys by electrodepositing alternating thin films of the constituents has been known to substantially improve a material's mechanical properties even more and is capable of producing virtually stress-free deposits when elements with essentially identical crystal structure and atomic radius are used [4, 5]. Modulation of thin films 10 - 100 nm thick to produce a metallic alloy is known as "nanolamination." Nanolaminates possess exceptional resistance to crack growth because delamination tends to occur at the layer interfaces or in the softer layer instead of alloying the crack to propagate straight on through, as a monolithic alloy does [6].

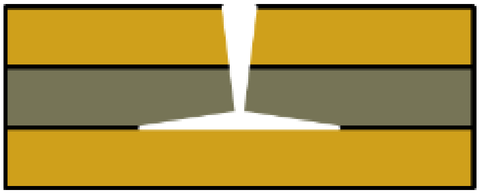

Figure 1. Crack redirection in a nanolaminated metallic system

In much the same way, pitting corrosion preferentially propagates along the layers that are less corrosion resistant of the two phases instead of propagating in an uninhibited unidirectional fashion, giving nanolaminated alloys superior corrosion resistance compared to their monolithic counterparts, as illustrated in Figure 2 [7, 8].

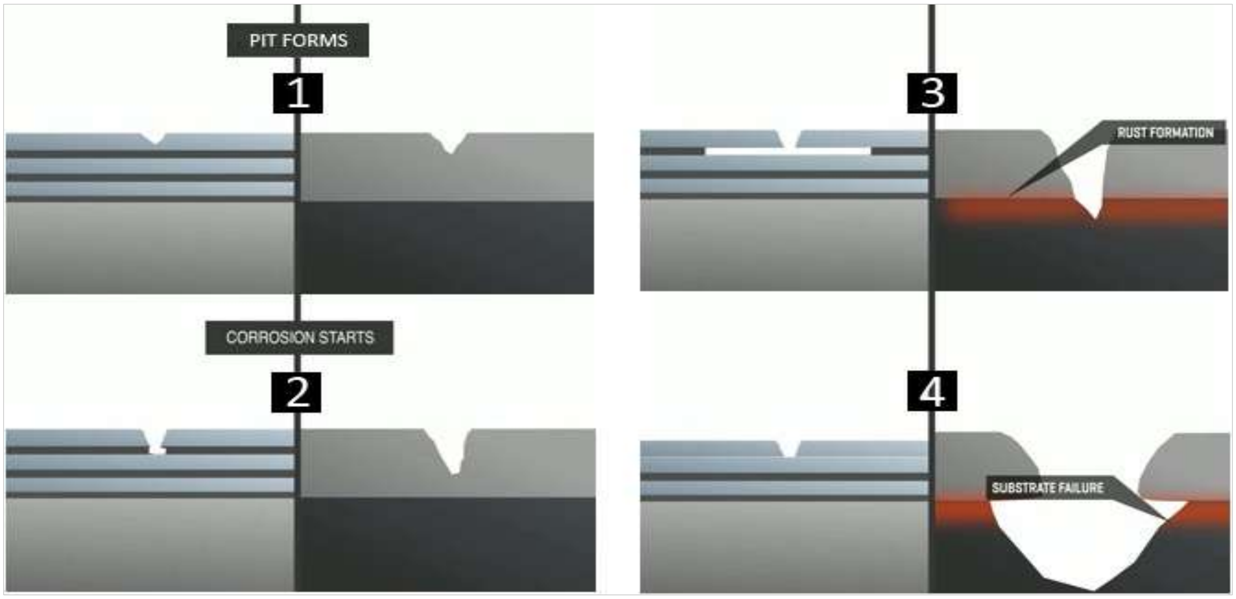

Figure 2. Comparison of pitting propagation in nanolaminate (left) vs. monolithic alloys (right) in a corrosive environment

Copper-nickel (Cu-Ni) nanolaminated coatings, especially containing ~70 wt% Ni, appear to be a particularly promising material for corrosion-resistant applications since nickel is often used already to extend the lifespan of copper tubing in marine environments, and use of bulk copper-nickel alloys is common and effective in severely corrosive environments [9, 10, 11, 2]. In a 2006 study by Ghosh *et al.*, it was found that nanocrystallinity of both monolithic and nanolaminated versions of Cu-Ni deposits contributed to superior corrosion resistance in room temperature 3.0 wt% NaCl solution compared to Monel 400 [12]. The high density of grain boundaries in the nanocrystalline materials caused more uniform pitting across the sample surfaces rather than a few deep pits that were localized along grain boundaries in polycrystalline Monel.

Creating nanocrystalline grains by electrodeposition is popular in the scientific community because the process essentially eliminates the prevalent pores and microstrain associated with mechanical methods of creating nanocrystallinity in materials, and the process makes it easy to enhance the material with nanoscale lamination as well [1]. Electrodeposition is favored over physical vapor deposition (PVD) in particular because of the inherent lack of stress that occurs in many electrodeposits [13]. The more compact morphology of electrodeposited nanolaminates is a source of enhancement for a variety of mechanical properties. Electrodeposition also has the advantages of being cost-effective, capable of controlling deposit thicknesses at an extremely precise level (from hundreds of nanometers to tens of micrometers), can often incorporate environmentally-friendly bath solutions, and can produce smooth, uniform deposits at high rates.

1.2. Basics of Electrodeposition

Alloys obtain a nanolaminated structure when the current density is modulated during galvanostatic electrodeposition so that only one constituent is preferentially-deposited at a time. Nickel deposits easily under activation or charge-transfer control over a wide potential range, but deposition of copper is limited by mass-transport control, so for nanolaminated Cu-Ni alloys, a high current density is used to deposit Ni-rich layers, and a lower current density is used to deposit Cu-rich layers [1, 14]. Current density modulation requires that a pulsed current (alternating, square waveform shown below) be applied rather than a direct current (straight, horizontal line waveform), as shown in Figure 3.

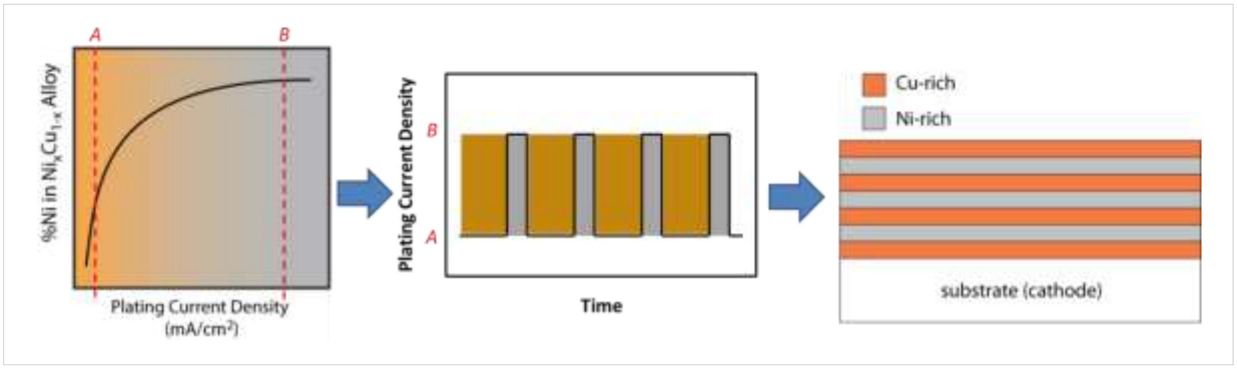

Figure 3. Nanolamination created in Cu-Ni alloys by current density modulation during electrodeposition

The pulsed current is applied with the anode and cathode (sample substrate) connected through a power supply and through the electrolytic plating bath, seen in Figure 4, to deposit a metallic film of constituent “M.” In the case of nanolaminated Cu-Ni alloy, the metals are reduced by Equations 4 and 5.

$$\mathrm{Cu}^{2+} + 2\mathrm{e}^- \rightarrow \mathrm{Cu} \qquad \text{(Equation 1)}$$

$$\mathrm{Ni}^{2+} + 2\mathrm{e}^- \rightarrow \mathrm{Ni} \qquad \text{(Equation 2)}$$

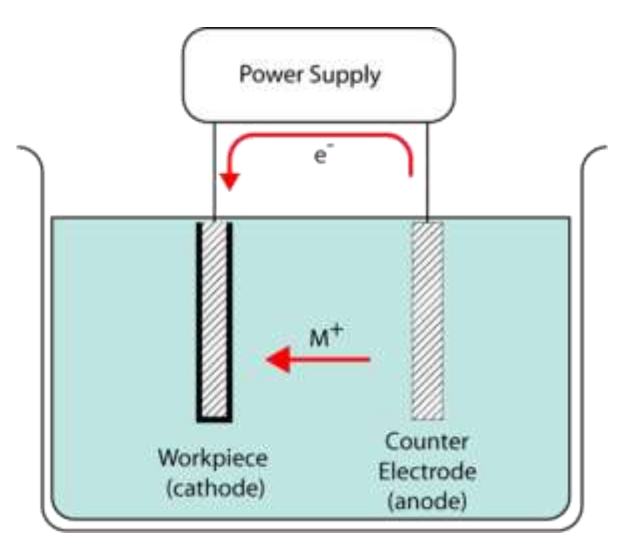

Figure 4. Electrodeposition set-up for plating a cathodic substrate with metallic deposit "M"

Sodium saccharin is often used as a grain-refining agent in the electrolytic bath and is known to reduce surface roughness in deposits by promoting planar grain growth instead of localized growth during the plating process [14]. Coumarine and polyethyleneglycol are other grain-refining agents that are commonly used [14].

1.3. Motivation and Objectives

The motivation in this project was threefold: 1) understand how processing affects microstructure to achieve desired mechanical properties, 2) develop characterization methods for Cu-Ni nanolaminates, and 3) contribute to a larger nanolaminate study in the Flinn research group on the structure-process-property relationships of the Cu-Ni nanolaminate system created by pulsed current rotating disk electrodeposition (RDE).

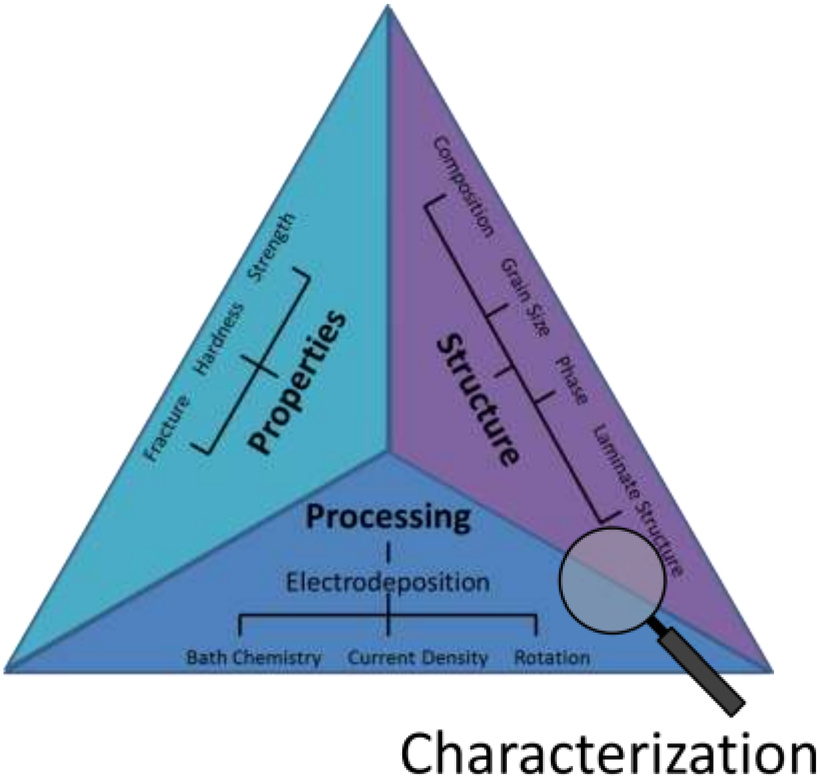

Figure 5. Motivation: characterization of the Cu-Ni nanolaminate system relating processing to structure

The objectives were to characterize the microstructure of the nanolaminate in terms of composition, grain size, phases, and laminate structure. Most studies in published literature focus on determining potential applications of Cu-Ni nanolaminates and ways to optimize properties by tailoring layer thicknesses and compositions, so the effects of RDE on Cu-Ni nanolaminate microstructure are not well known. Cu-Ni was chosen for this study because it is a common model system for studying electrodeposition of metals in a modulated structure and it is a system whose electrochemical behavior is well-characterized in literature [15]. X-ray diffraction (XRD) was used to determine overall deposit compositions, phases, and grain sizes. Scanning electron microscopy (SEM) was used to examine the grain structure, phases, and laminate microstructure. Energy dispersive X-ray spectroscopy (EDS) was utilized to determine overall compositions in comparison to XRD data.

Method	Composition	Grain Size	Phases	Laminate Structure
XRD	✓	✓	✓	
SEM		✓	~✓	✓
EDS	✓			

Figure 6. Characterization methods used to examine structural properties in the Cu-Ni nanolaminate system

1.3.1. Composition

No literature studies incorporating the same plating conditions as those used to create the samples in this study could be found, and none from the literature review identified specific layer compositions of the nanolaminated coatings. A coating that is deposited on a rotating substrate during electrodeposition (rotating disk electrode set-up) experiences current crowding around the edges of the sample. In this study, compositions of both nanolaminate layers were determined, with the Ni-rich layer composition measured from a representative sample of monolithic Ni-rich deposit. Copper content of the Cu-rich layers was calculated using the following mass balance equation:

$$C_{Cu}^{Cu-rich} = \frac{\left(C_{Cu}^{bulk,nl}\right) - \left(V_f^{Ni-rich}\right)\left(C_{Cu}^{Ni-rich}\right)}{\left(V_f^{Cu-rich}\right)} \qquad \text{(Equation 3)}$$

where *C* is a composition, subscripts of *C* represent elements of interest, and superscripts represent the phase from which the element of interest exists. V_f values are volume fractions of the phases indicated by superscripts. Because the only dimension that differs between Cu-rich layers and Ni-rich layers in SEM images is the layer thickness, thickness fractions (layer thickness divided by bi-layer thickness) were used.

XRD was the primary characterization method used to determine compositional data because selectively etching SEM/EDS samples for visual contrast can alter the composition of a sample at the surface. EDS data from a previous study in-house examining unetched samples from the same nanolaminated and monolithic deposits were provided for analysis.

The XRD shoots a focused X-ray beam onto the sample, which scatters electrons out of atoms which lie in crystal lattice planes. The intensity of energy from the scattered electrons and the angle between the incident and scattered beam are measured by a detector. Intensity is then plotted on a computer as a function of this angle (2-θ) as a diffraction pattern, where Bragg angle (θ_B, half of 2-θ where diffraction peaks occur) is related to the X-ray radiation by Bragg's Law [15]:

$$\lambda = 2\, d \sin\theta_B \qquad \text{(Equation 4)}$$

λ is the wavelength of Cu-Kα X-ray radiation (1.54 Å) from the XRD.

Peak intensities and locations can reveal crystal structure and elemental identification by matching the spectrum to MDI Jade software's collection of peak profile databases. From there the program can calculate elemental compositions in wt% and at% from the matches. Unfortunately, the databases only include profiles for powder diffraction samples. The X-ray beam tends to diffract differently between powders and solid samples because powders create more opportunity for the beam to scatter electrons from a variety of crystal planes, and therefore powdered spectra tend to be more intense at preferred orientations in the diffraction spectrum. The profiles are capable of providing a reasonable match for solid samples, but the relative intensities between diffraction peaks do not always remain a good fit to those of an equivalent powdered sample.

In addition to calculating elemental composition by peak fit profiles, composition can also be obtained from the lattice constants measured by XRD. The lattice constant for pure Ni is 3.523 Å, and 3.615 Å for pure Cu. The values seen in Baskaran *et al.* for monolithic Cu-Ni samples were 3.541 – 3.623 for 1.85 – 60.1% Ni alloys [16]. The lattice constant increased in size with increasing Cu content. The same trend was observed by Agarwal *et al.*; the lattice parameters of their samples were a precise fit to Vegard's law, in which the lattice constant of the interstitial solid solution is directly proportional to the atomic percent solute present [2, 15]. The same trend was expected in the samples of this thesis, with lattice constants remaining between those of pure Ni and pure Cu along the theoretical line of Vegard's law in Figure 7.

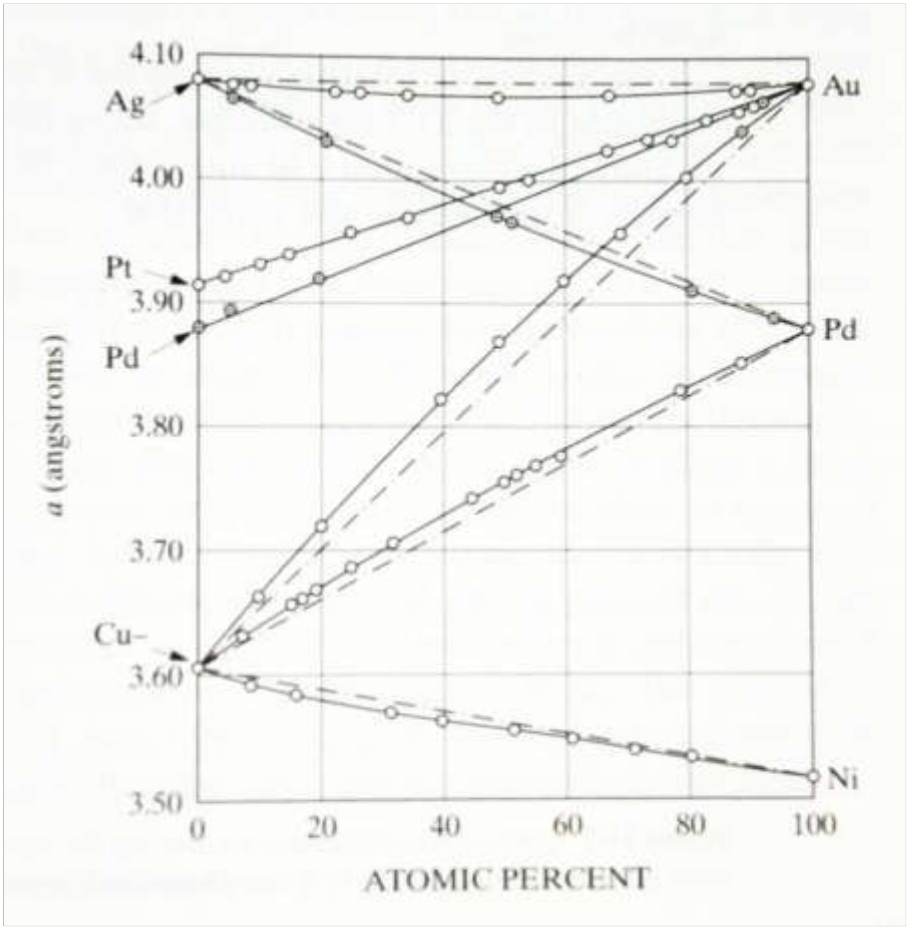

Figure 7. Lattice constants of some metallic solid solutions based on Vegard's law (dot-dash line)

From the lattice constants of Cu and Ni, Vegard's law describes the lattice constant, *a*, of a Cu-Ni interstitial solid solution as a function of at% Ni, *X*, by Eqn. 3.

$$a = -0.0009\,X + 3.615 \qquad \text{(Equation 5)}$$

1.3.2. Grain Size

Peak widths (full width half max, or FWHM values) in XRD spectra are dependent on grain size, where generally a broader peak corresponds to smaller the grain size according to Scherrer's formula [17]:

$$D = \frac{0.9\,\lambda}{B\cos\theta_B} \qquad \text{(Equation 6)}$$

where *D* is the crystallite size, λ is the X-ray wavelength, *B* is the width of the diffraction curve (the full width half max, or FWHM, of a peak in a sample's XRD spectrum), and ϑ_B is the Bragg angle. In studies with samples produced under similar conditions to those used in this research project, crystallite sizes of 18-31 nm [2] and 20-50 nm have been reported for nanolaminated samples [18], and ~29 nm for monolithic Ni-rich alloys of copper and nickel [1]. A slightly Cu-rich monolithic deposit ($Cu_{55}Ni_{45}$) had a reported crystallite size of 26 nm [1]. From literature reviews, it appears that nanolamination of Cu-Ni introduces a wider range of grain sizes compared to the monolithic alloy.

1.3.3. Phase Identification

Baskaran *et al*. published a study in 2006 showing changes in XRD spectra for electrodeposited Cu-Ni alloys in monolithic compositions ranging from Ni-rich to Cu-rich corresponding to current densities of 2.5 – 20 A/dm^2 (25 – 200 mA/cm^2) and compositions from $Cu_{0.38}Ni_{0.62}$ (60.1 wt% Ni) to $Cu_{0.98}Ni_{0.02}$ (1.85 wt% Ni) [16]. While the plating conditions differed from those of this thesis, a trend in XRD spectra was observed in Figure 8, where peaks decreased in intensity with increasing current density, and the difference in relative height between the (1 1 1) peak and (2 0 0) peak (the two significant peaks for an FCC material) increased with current density. This relationship between composition and diffraction peak intensity seemed like a feasible expectation for XRD data: as composition changes, so should peak intensities. No distinct peaks were visible for pure Ni or Cu phases because of peak shifting indicative of the formation of a solid solution. Indeed, all phases identified by the authors' spectra database were alloys of Cu-Ni, which is reasonable for an electrodeposited monolithic alloy.

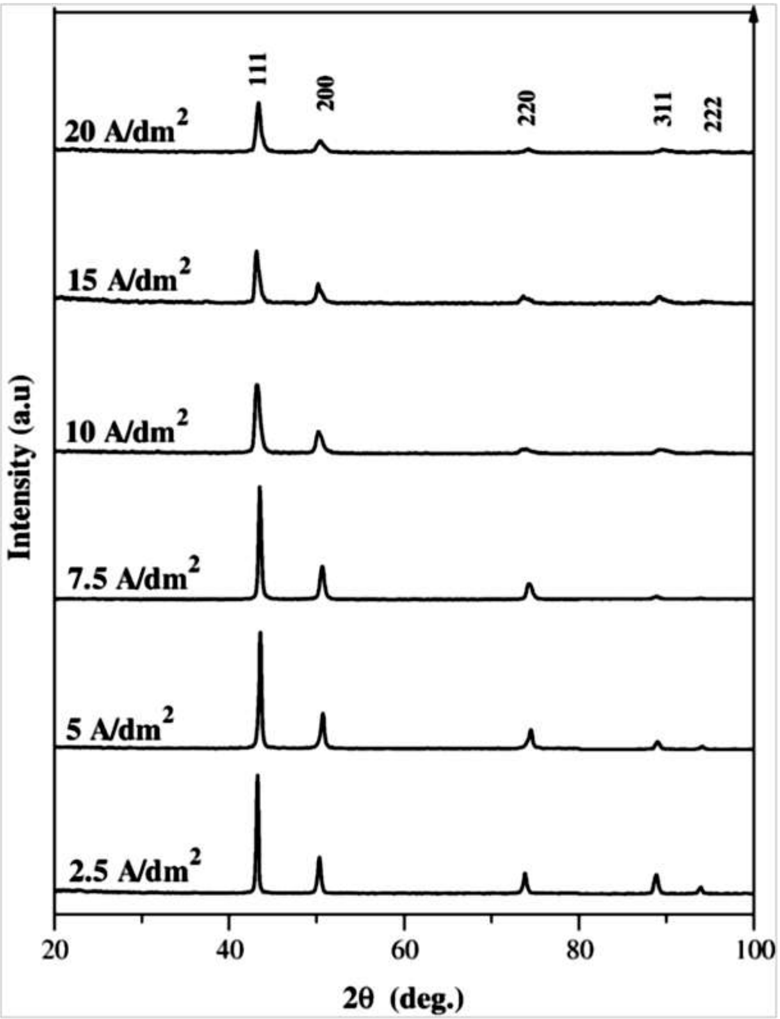

Figure 8. XRD spectra for nanolaminated Cu-Ni films deposited with varying current density [Baskaran 2006]

The peak locations confirmed a face-centered cubic (FCC) crystal structure, which corresponds also to the FCC nature Cu and Ni. Peaks also seemed to broaden with increasing current density corresponding to decreasing copper content and grain size.

Bonou *et al.* observed a similar Cu and Ni peak shift and overlap in their nanocrystalline, monolithic Cu-Ni samples as well. The authors included vertical lines indicating where the peaks of pure Cu and pure Ni would normally be to qualitatively show that interstitial solid solution strengthening caused the peaks to shift [19].

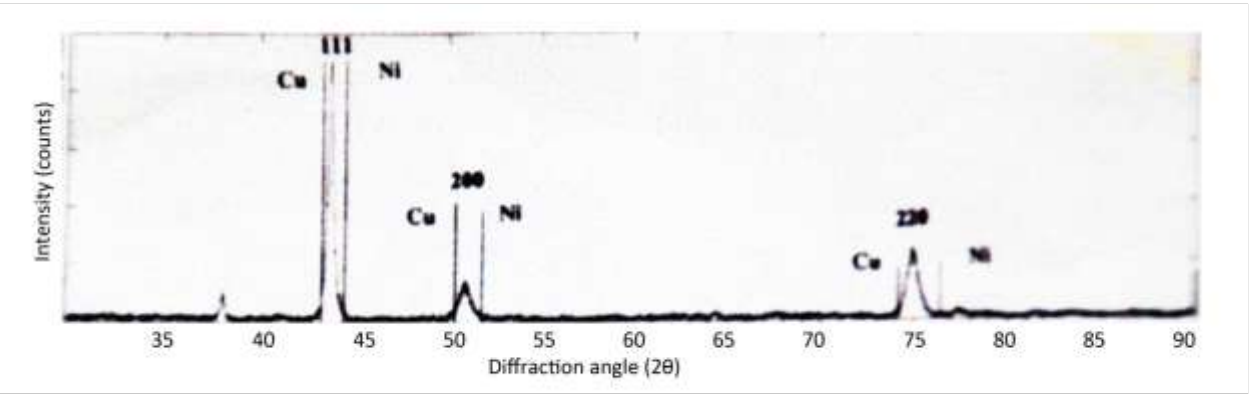

Figure 9. XRD spectrum for monolithic Cu-Ni showing locations of pure constituent peaks in relation to those of the alloy [Bonou 1994]

Agarwal *et al.* tested monolithic Ni-rich Cu-Ni films electrodeposited in a plating bath very similar to the one used in this study, though their plating bath did not contain a grain-refining agent like sodium saccharin and the authors used a pulsed current of various current densities and off-time (so the Ni-rich composition was only deposited while current was running, and nothing was deposited at the bottom of the waveform when no current was running). Like the Baskaran article, peak-shifting instead of distinct and disparate Cu and Ni peaks was observed and attributed to interstitial solid solution strengthening in the Cu-Ni coating [2].

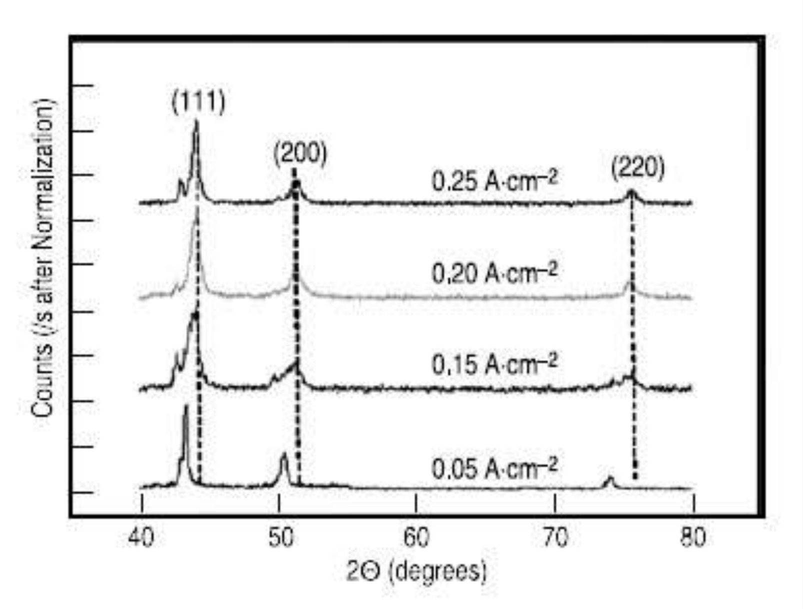

Figure 10. XRD spectrum of monolithic Ni-rich deposits made with pulsed current and varying current densities [Agarwal 2010]

Rajasekaran *et al.* produced pulse current electrodeposited nanolaminated Cu-Ni coatings in a 2009 study, and observed distinct peaks for Cu and Ni (Figure 11) instead of peak overlaps that might indicate alloying of the constituents. The authors noted that the overall composition in their samples was 62% Cu and 38% Ni [18]. Evidence of distinct Cu and Ni spectra in the same diffraction pattern is logical considering that the nanolaminate is essentially only alloying interstitially at the layer interfaces and to the substrate.

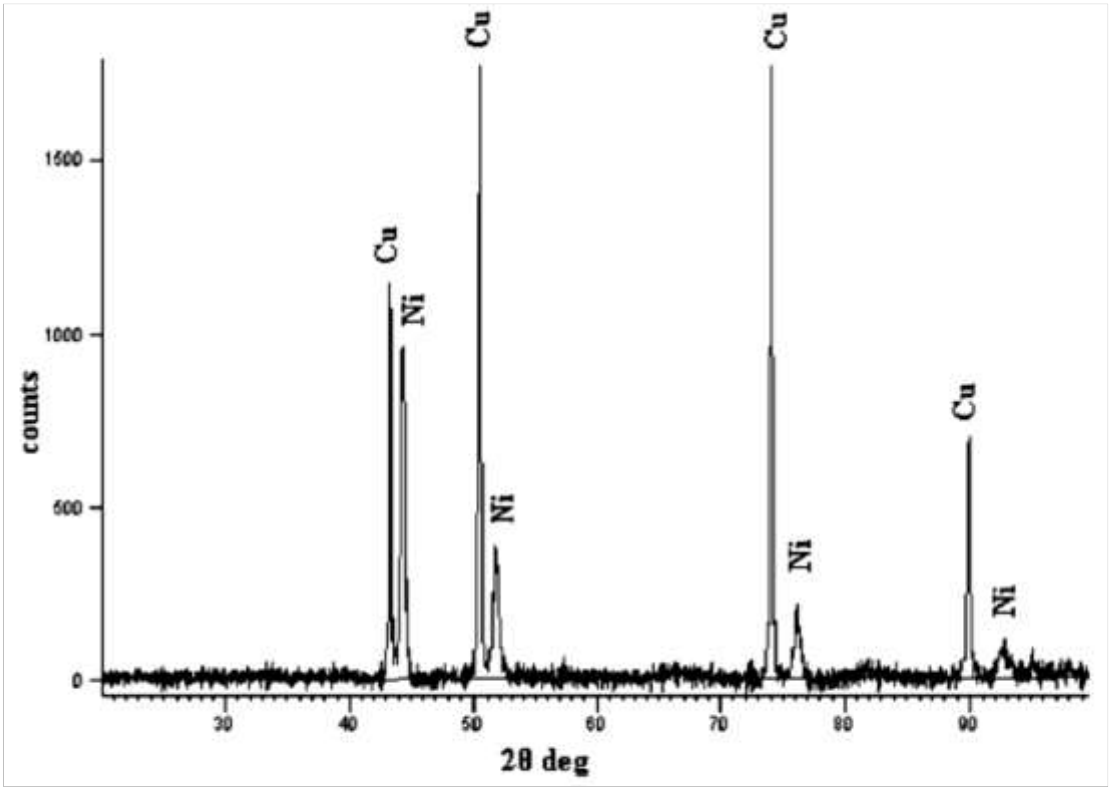

Figure 11. XRD spectrum for nanolaminated Cu-Ni films [Rajasekaran 2009]

Ebrahimi *et al*., which electrodeposited nanolaminated thin film samples from a boric acid based plating bath and pulsed current, also observed distinct Cu and Ni peaks in their XRD sample spectrum, but with noticeable peak overlapping (Figure 12). (1 1 1) and (2 0 0) textures for FCC Cu and Ni were still evident in the diffraction pattern [20].

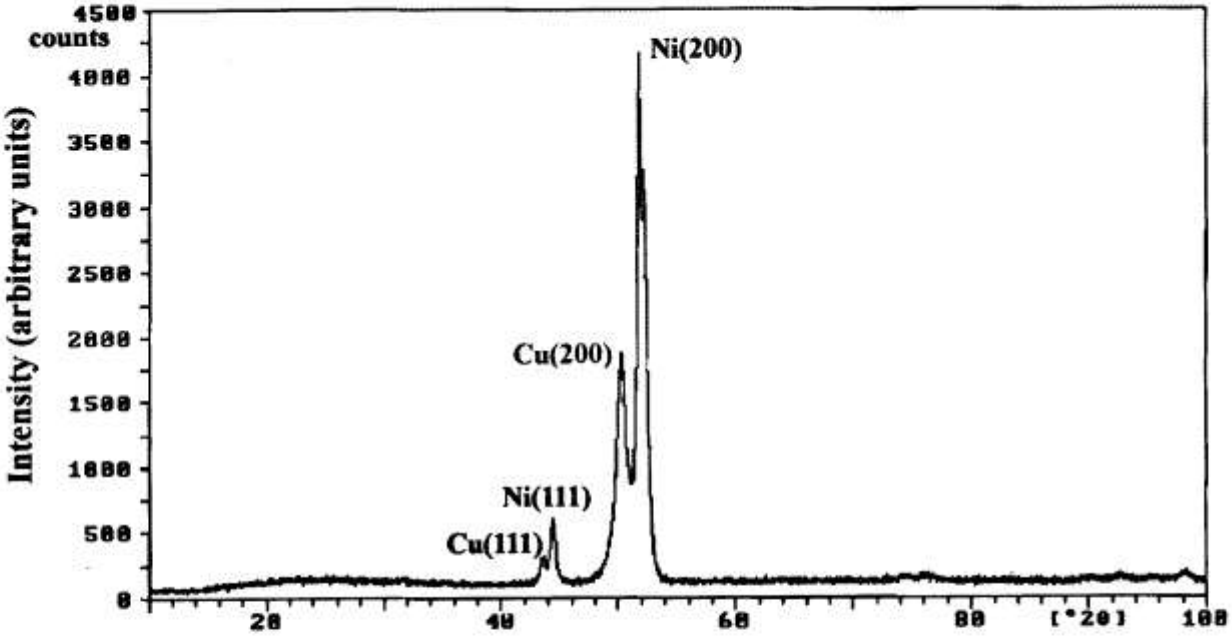

Figure 12. XRD spectrum for nanolaminated Cu-Ni from [Ebrahimi 2001]

The authors did not quantify the elemental composition in their samples, but in comparison to the more defined Ebrahimi spectrum, it was postulated that perhaps this discrepancy is due to the differences in X-ray beam spot sizes associated with different XRD models. Neither article stated which specific XRD model was used, but some units have focal spot sizes larger than 0.5 mm and some have sizes even smaller than 50 microns, with all sizes in between possible as well [21]. It is possible that the smaller the beam, the more likely it is to identify phases that are highly Cu-rich or Ni-rich, and the larger the beam, the more likely the machine is to recognize several phases as one solid solution of Cu-Ni. The Materials Science & Engineering (MSE) department at the University of Washington (UW) uses a Bruker D8 Focus model, and Bruker does not list a focal spot size for the X-ray beam on their website. Tuesday Kuykendall, the MSE lab manager at UW, presumed that the spot size of the D8 Focus would likely be much too large to identify distinct Cu-rich and Ni-rich phases in the sample coatings because the layers of each phase were only 100 nm thick. As such, the Ebrahimi spectrum was considered more relevant to this study than that of Rajasekaran, and the large peak overlaps/shifts of Agarwal and Baskaran were predicted for the spectra of the monolithic samples in this thesis.

1.3.4. Laminate Structure

Most studies found in literature concerned optimizing the surface morphology of the electrodeposited samples rather than observing cross-sectional laminate morphology of the coatings because properties like hardness and corrosion resistance are dependent on having the smoothest, most uniform surface possible. Therefore, little was known about what the microstructure of samples from this study should look like. With etching, contrast was expected between Cu-rich and Ni-rich layers under the SEM similar to what Kaneko *et al.* published in 2005 (Figure 13).

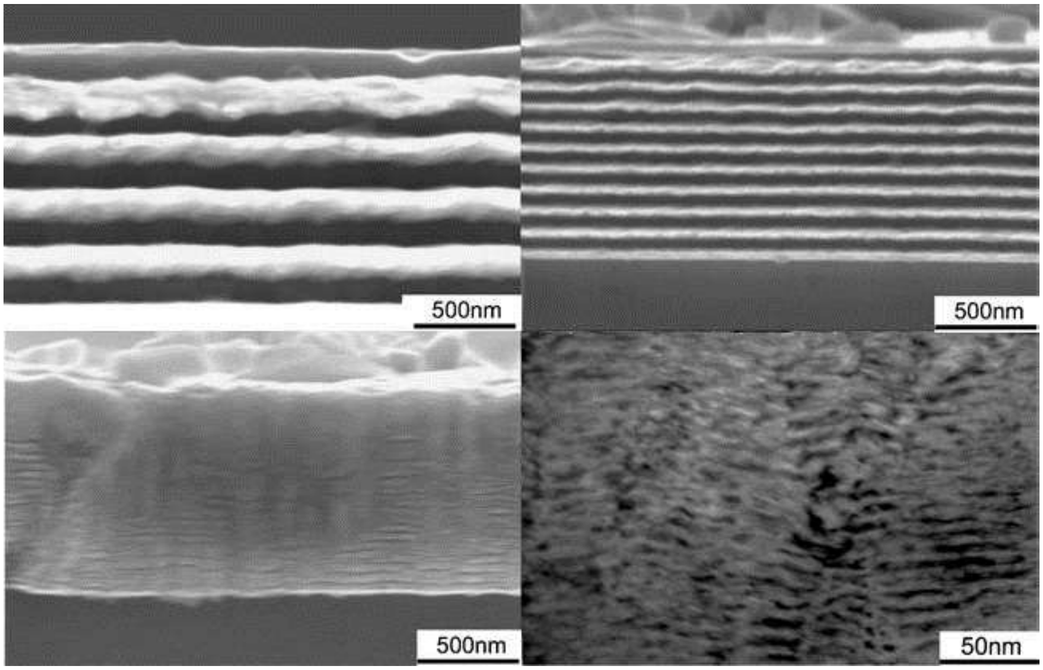

Figure 13. SEM images of layers in a nanolaminated Cu-Ni coating [Kaneko 2005]

Because the microstructures are smaller than 100 nm, it was uncertain whether or not the SEM model used in this study, a JEOL JSM-7000F, would be capable of resolving structures within the layers. Although SEMs exist that are capable of resolving structures as small as ~3 nm (Figure 14), the JEOL website sites the electron beam resolution as only 10 nm with secondary electron imaging [22]. The grain sizes of 18-50 nm from the literature review indicated that SEM would be capable of resolving microstructures potentially as small as the grains.

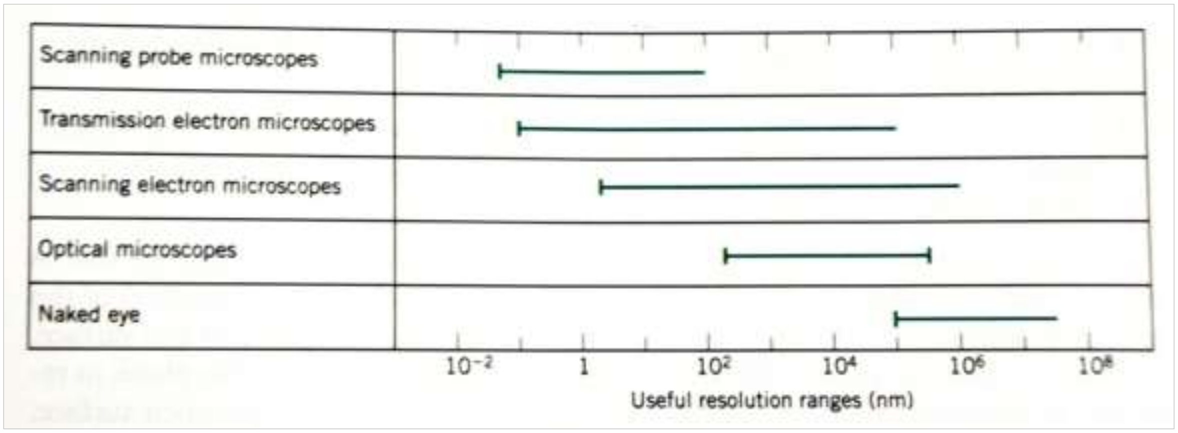

Figure 14. Microscopy resolution ranges

Theoretically speaking, the use of sodium saccharin in a Cu-Ni plating bath is effective at ensuring relatively uniform grains in deposits during pulsed current electrodeposition and is known to promote the formation of spherical grains (which corresponds to the nodular coating surfaces that as-deposited samples typically have) [23, 7]. Saccharin-free plating baths tend to produce more faceted and columnar grains [1, 24] (Figure 15).

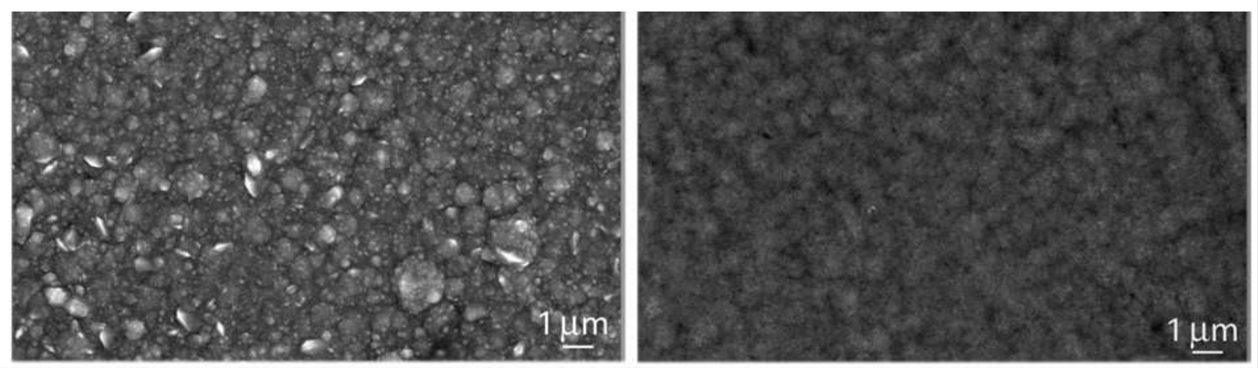

Figure 15. SEM images of as-deposited monolithic nanocrystalline Cu-Ni alloys from (left) a saccharin-free plating bath and (right) saccharin-containing bath [Pellicer 2001]

2. Materials

All samples were created by Bradford Duvall, a former member of the Flinn research group in the Materials Science & Engineering department at the University of Washington, in an outside lab. Monolithic and nanolaminated coatings were deposited polished polycrystalline copper substrates (1.5 x 1.5 inches / 38 x 38 mm in size; ~14.516 cm^2) from a 900 mL plating bath composed of the following constituents in deionized water: 0.025 M copper sulfate, 0.7 M nickel sulfamate, 0.25 M sodium citrate, 2.3 g/L sodium saccharin, and 0.15 g/L sodium dodecyl sulfate (SDS). A spike solution of 0.5 M copper sulfate in deionized water was added periodically to replace depleted copper in the plating bath. Bath pH was ~4.0. Samples were plated in a rotating disk electrode set-up with rotation speed maintained at 160 rpm and a direct current density of 40 mA/cm^2 for the monolithic Ni-rich sample. The laminated sample was plated by pulse current modulated between 40 mA/cm^2 for the Ni-rich layers and 10 mA/cm^2 for the Cu-rich layers and rotation speeds of 160 and 500 rpm, respectively. The surface of the nanolaminated sample had evident swirl marks from the alternation of rotation speeds as shown in Figure 16.

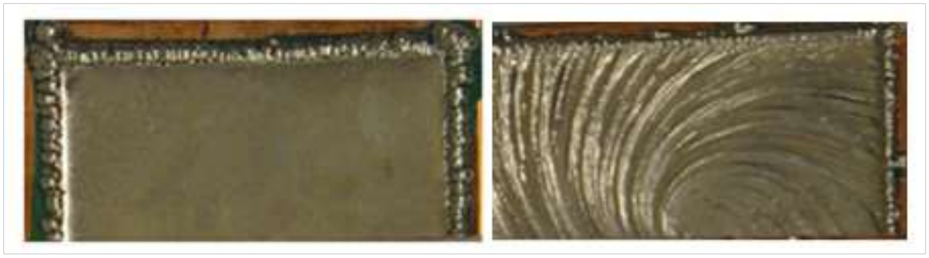

Figure 16. As-deposited coating surfaces from rotating disk electrode samples (*left*: monolithic nickel; *right*: nanolaminate)

Pulse periods in the nanolaminated sample were such that layers of ~100 nm were produced and plating times for both samples were such that coatings were ~500 µm thick. Part of the coating thickness in the nanolaminated sample consisted of a Ni-rich top coat ~150 µm thick, which was intended to help produce a sharp crack in future fracture testing. These two square electrodeposited samples were cut into rectangles for XRD testing as well as several small beams originally meant for fracture testing.

3. Experimental Procedures

3.1. X-ray Diffraction

A Bruker D8 Focus X-ray diffractometer (XRD) with copper-Kα radiation was used at a working power of 40 kV and 40 mA. The monolithic Ni-rich sample for XRD was 17 x 6 x 1.5 mm in size, and the nanolaminated XRD sample was 17 x 4.5 x 1.5 mm in size. Each sample was mounted on a square poly(methyl methacrylate) (PMMA) XRD sample holder with a small amount of clay to keep the sample level with the top edges of the sample holder. The samples and holders were oriented such that the X-ray line beam would hit the samples length-wise at the coating (Figure 17).

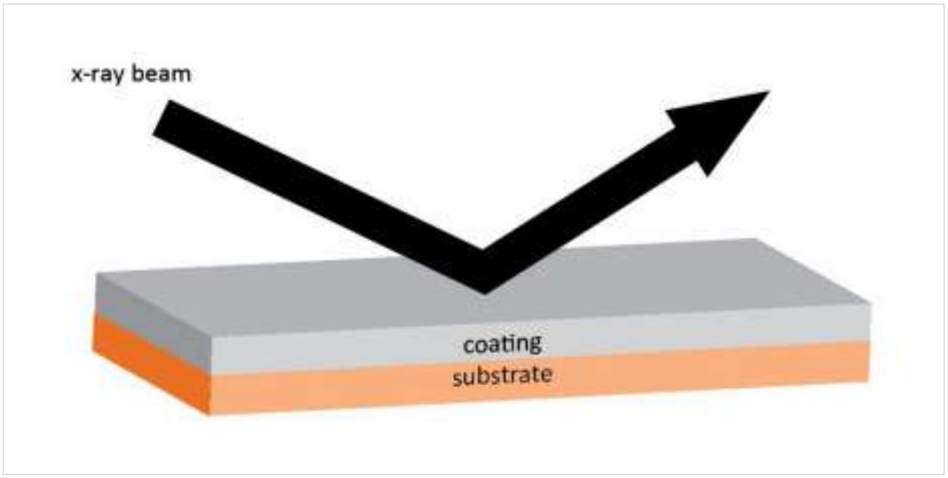

Figure 17. Orientation of XRD samples during testing

The swirled surface of the nanolaminated sample was ground smoother with 600 grit sandpaper to reduce background noise in subsequent XRD spectra and to remove the Ni-rich top coat that would have interfered with compositional analysis of the nanolaminate. The sample surfaces were relatively flat, as evident in Figure 18.

Figure 18. Nanolaminated and monolithic X-ray diffraction samples

Spectra were collected from $2\theta_{hkl}$ between 40 and 80°, with a 1 sec/step collection rate and a step size of 0.05°. A 0.2 mm divergence slit, 0.6 mm anti-scattering slit, and 0.6 mm detector/receiving slit were used. All spectral analysis was performed with MDI Jade software and diffraction spectra database.

3.2. Sample Preparation

All nanolaminate beams were cut with a low-speed diamond saw from the same electrodeposited sample, but specifically from either a region that experienced lower current density (toward the center of the square sample) or higher current density (toward the edges of the square sample where current crowding had occurred) during electrodeposition. Beams were 8 x 1.5 x 1.5 mm in size. One of each type of beam was restrained by coiled aluminum clips, oriented so that a beam cross-section would be visible, and the beams were mounted into the first of three red bakelite pucks with diameters of approximately 31 mm. One of each beam was also mounted, substrate side down, into another red bakelite puck, with a small amount of black bakelite included along one puck edge for quick sample identification since the samples were essentially mounted with two-fold symmetry. Small glass squares cut from microscope slides were inserted into the clips above the beams to hold the clips open more uniformly to ensure that the beams would lie flat during pressing. This puck was ground with a 240 grit polishing cloth to an angle of 18.82° so that the angle would reveal elongated grains and layers (as demonstrated in Figure 19) for easier SEM and EDS analysis.

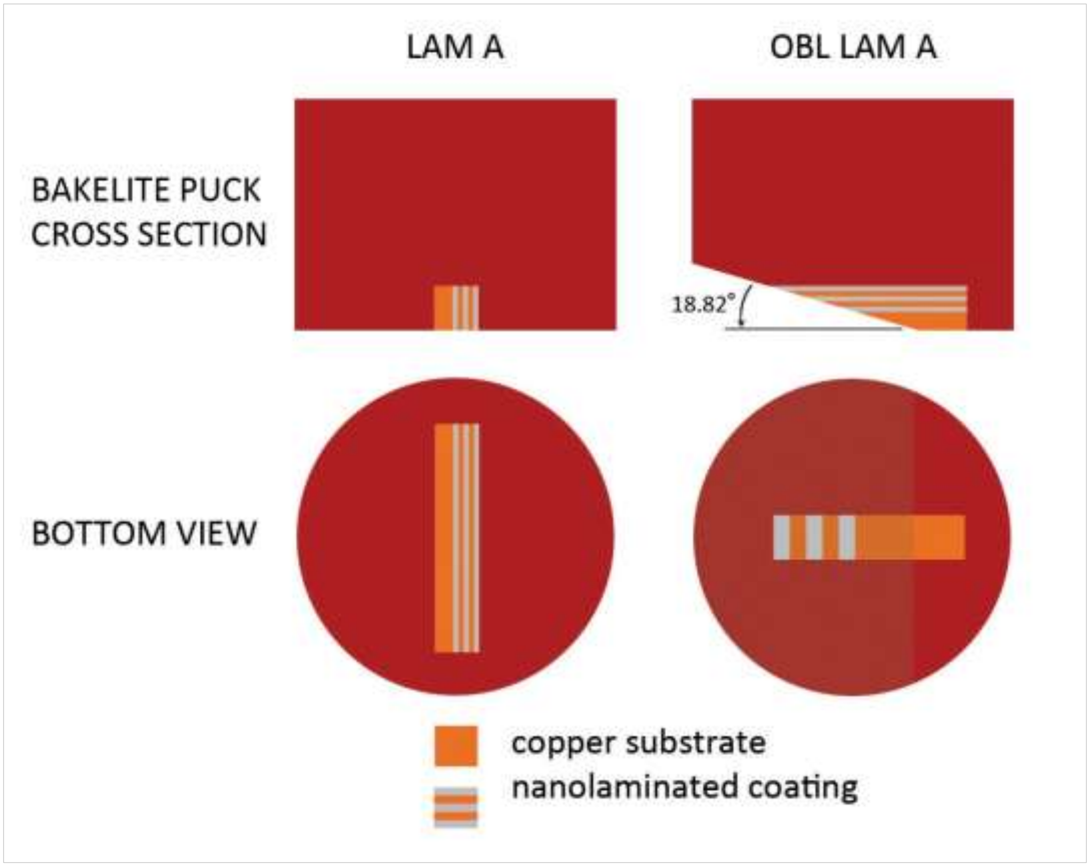

Figure 19. Diagram showing layer elongation created by angling the surface of the nanolaminated sample "OBL LAM A"

A third puck was created with a single beam of monolithic Ni-rich coating, oriented with the beam cross section visible. These pucks are shown in Figure 20 in the order that they were introduced.

Figure 20. Orientations of the electrodeposited sample beams mounted in bakelite pucks

From the first puck, the sample positioned at the top will be referred to as “LAM C,” the nanolaminated sample taken from a high current density region. Below it is “LAM A,” the nanolaminated sample from a low current density region. The second puck included LAM C on the left and LAM A on the right, but the LAM C beam became dislodged after polishing so it was not available for analysis. LAM C on the puck with the oblique surface was aptly named “OBL LAM C.” The monolithic Ni-rich sample in the third puck was simply named “MONO” during testing for its monolithic composition.

All samples were initially ground flat on a polishing wheel with 400 grit, 600 grit, and 1200 grit sandpaper rotating at 300 rpm. Samples were then polished to a glossy finish with the wheel rotating at 150 rpm and the following order of polishing cloths and alumina polishing media: 9 µm, 3 µm, 1 µm, 0.05 µm, and 0.01 µm. Pucks were sonicated and rinsed in deionized water before moving on to each successive polishing cloth.

No contrast between copper and nickel layers was visible under SEM (with either secondary electron imaging or electron backscattering) after just polishing, so various wet etchants were used to selectively etch either copper or nickel in the coatings. Etchants of varying concentrations of HCl with and without sonication caused significant pitting when the nanolaminated samples were immersed for times of five seconds to one minute. The samples were repolished between each etch. Light relief of copper grains and layers was produced in OBL LAM A by immersing it for five seconds in a solution of 5 mL NH_4OH (25-30 wt% ammonia), 5 mL deionized water, and 2 mL fresh 3% H_2O_2, as recommended by ASM International [25]. Deeper relief of layers was produced in the LAM A and LAM C samples by immersing the puck in a fresh solution of the same etchant for one minute. The monolithic nickel sample was etched by immersion for five seconds in a solution of 2 mL HNO_3 (68-70 wt%), 1 mL glacial acetic acid (99.7 wt%), and 1 mL deionized water, as recommended by Smithells Metals Reference Book for nickel-rich Cu-Ni electrodeposited alloys [26]. All pucks were thoroughly rinsed with deionized water until the pH of water on top of the pucks was neutral, as read from paper pH indicator strips. The pucks were then rinsed a final time before drying them under a pressurized stream of air.

3.3. Scanning Electron Microscopy and Energy Dispersive X-ray Spectroscopy

All samples were placed under house vacuum for at least 24 hours prior to SEM imaging. Carbon tape was placed across the top of each sample and the sample holder edges to prevent charging. A JEOL JSM-7000F model field emission scanning electron microscope was used for secondary electron imaging at accelerating voltages of 10-15 kV.

Quantitative chemical composition data was collected during SEM microscopy by energy dispersive X-ray spectroscopy (EDS). The spot mode function of EDAX Genesis was used for layer and microstructure analysis in the nanolaminated samples, but overall compositions were calculated for the entire computer screen view in the monolithic Ni-rich sample. Accelerating voltage in the SEM was held at 15 kV for all EDS analysis.

4. Results and Discussion

4.1. Laminate Structures from SEM

Initial images on the SEM of the interface between coating and substrate confirmed that the etchant could produce definition around copper grain boundaries and relief between Cu-rich and Ni-rich layers.

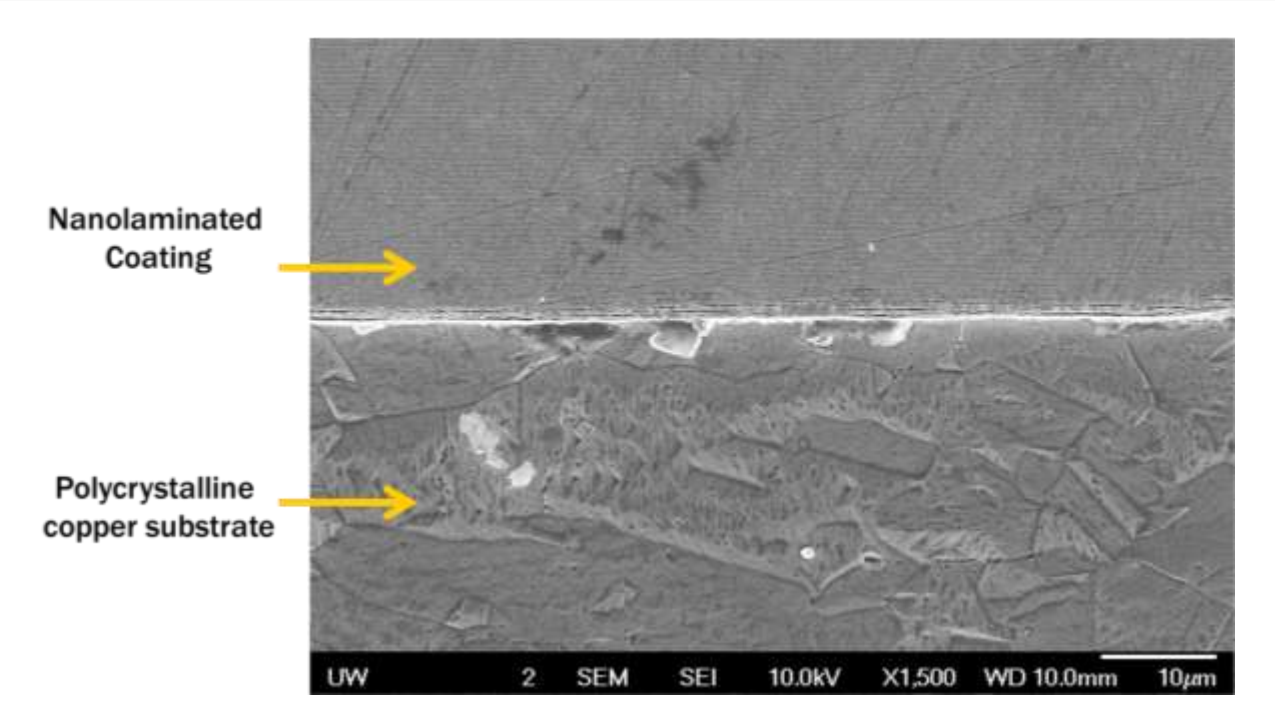

Figure 21. SEM image of etched polycrystalline copper substrate grains and contrast between coating and substrate

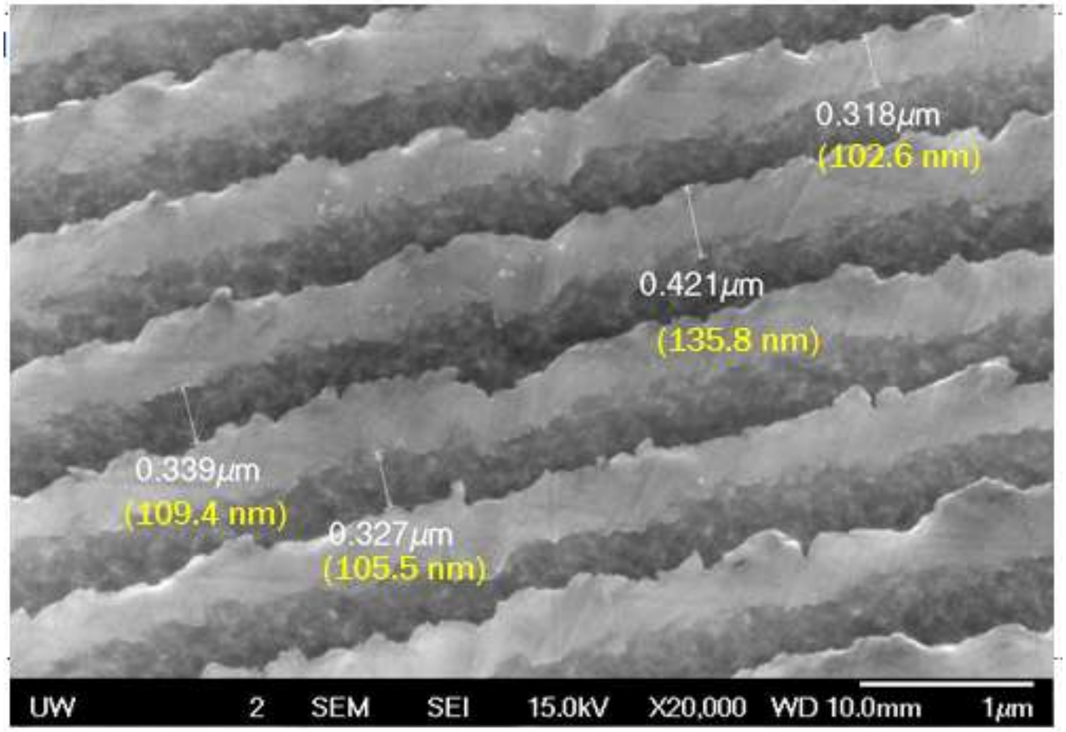

Figure 22. Measured and actual layer thicknesses on OBL LAM A under SEM at 20,000X magnification

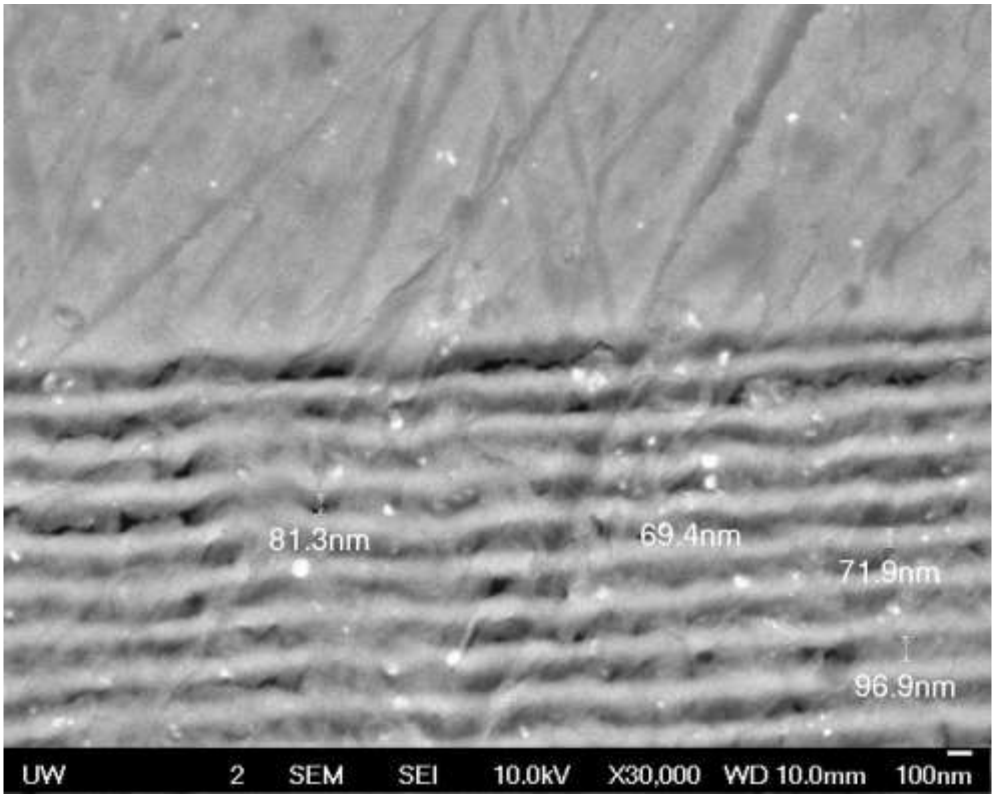

Figure 23. SEM images of measured layer thicknesses in LAM C at 30,000X magnification

Average layer thicknesses were observed to be ~103 nm in both Cu-rich and Ni-rich layers, with some as small ~70 nm and as large as ~135 nm.

Table 1. Average layer thicknesses and calculated volume fractions of each phase

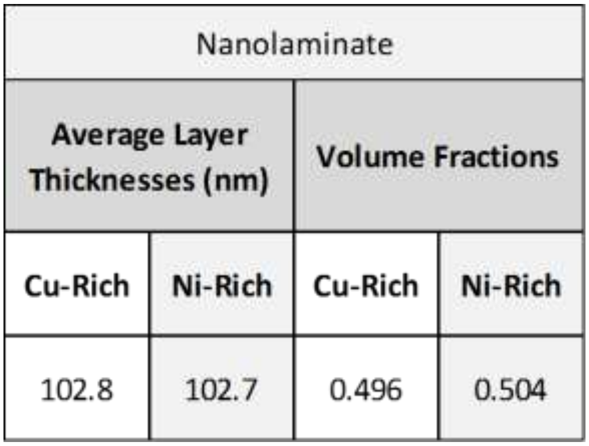

Nanolaminate			
Average Layer Thicknesses (nm)		**Volume Fractions**	
Cu-Rich	**Ni-Rich**	**Cu-Rich**	**Ni-Rich**
102.8	102.7	0.496	0.504

As such, the volume fractions of Cu-rich and Ni-rich layers were both estimated to be ~0.50.

Because macroscopic swirls were visible on the coating's surface after electrodeposition, reflections of this inconsistency were expected to be found within the deposit's microstructure.

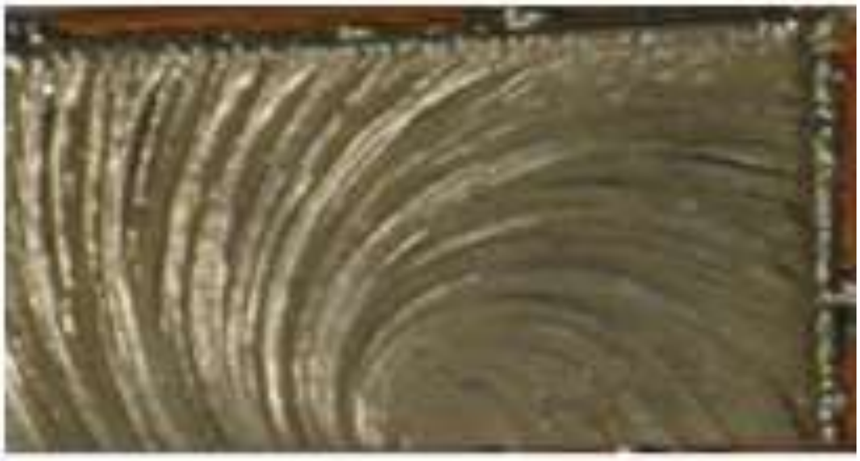

Figure 24. Macroscopic swirls in coating of nanolaminate deposit

Layer inhomogeneity was evident throughout the nanolaminate deposit under SEM. Copper-rich streaks, non-planar layers, and other defects were present in each nanolaminated sample.

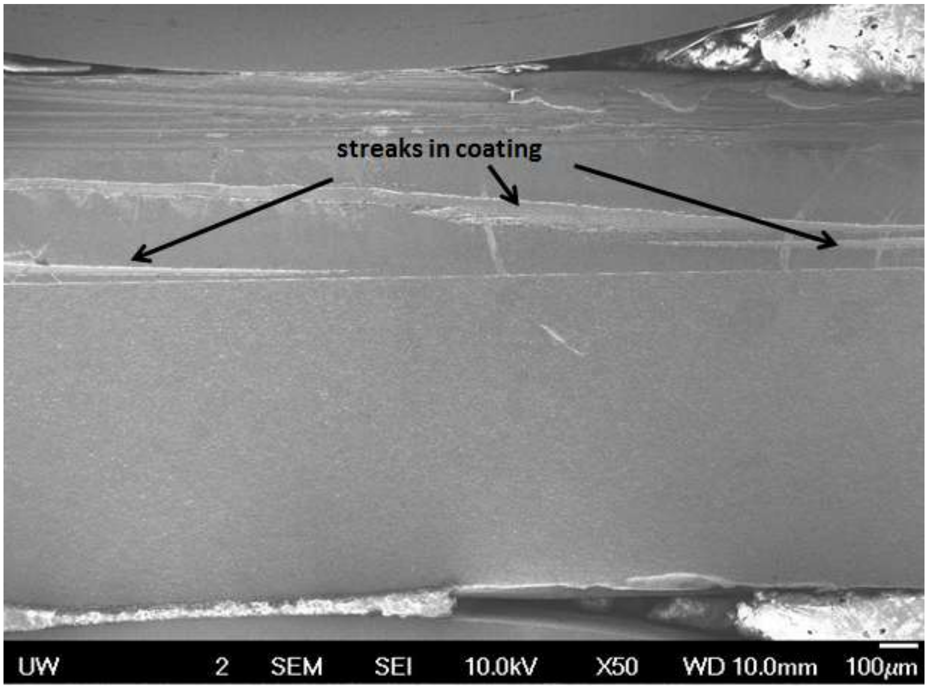

Figure 25. Streaks in nanolaminate coating (LAM A sample) at 50X magnification

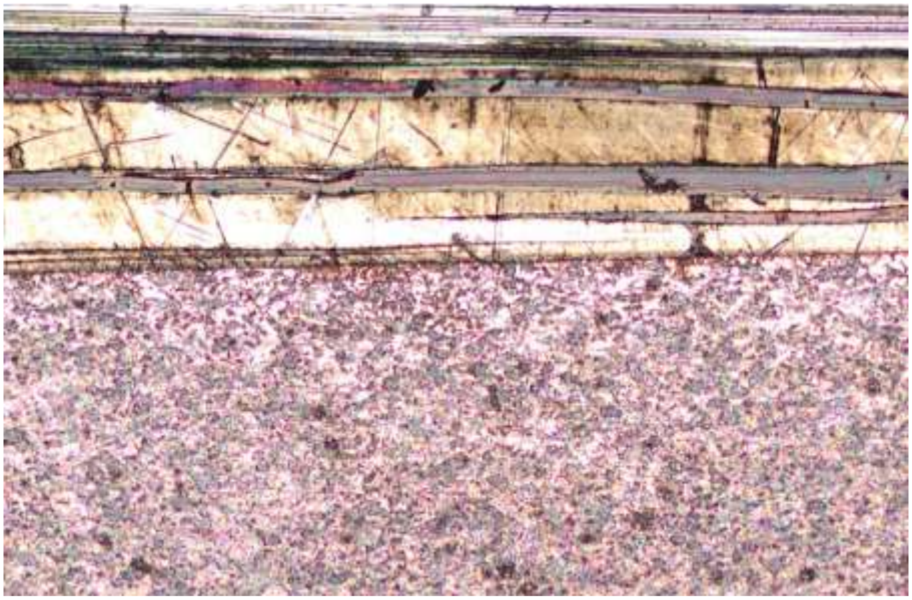

Figure 26. Optical micrograph of Cu-rich streaks seen across LAM A deposit at 5X magnification

The streaks appeared to be particularly disruptive to the planar orientation of the layers in OBL LAM A. The white string across the right, bottom corner of Figure 27 is a contaminant.

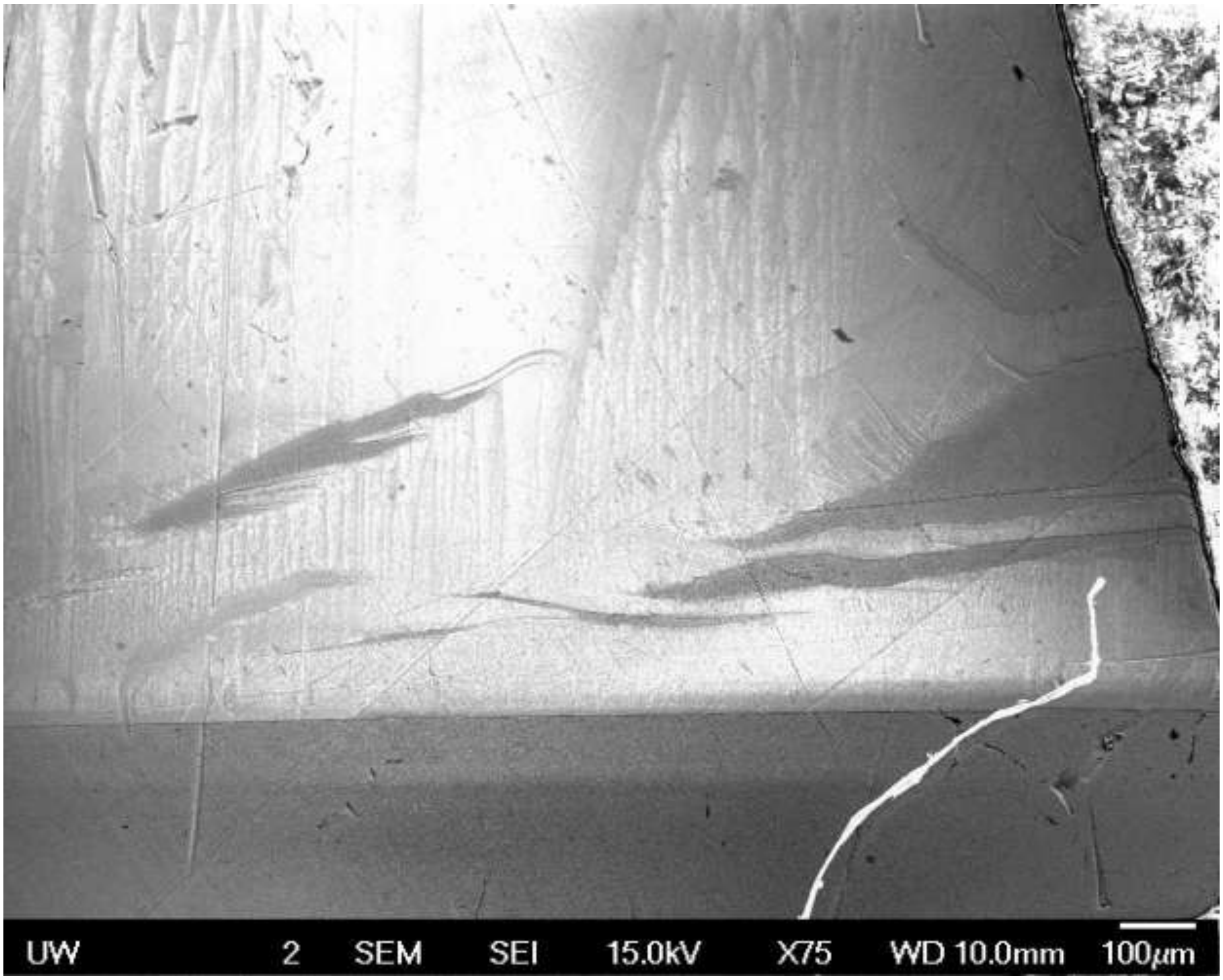

Figure 27. SEM image of OBL LAM A showing streaks in the coating and contrast

Magnifying the view to 1,000X (Figure 28), the streaks appeared to blend into the nanolaminate layers in the top section, but more abruptly halted the nanolaminate morphology in a step-wise fashion.

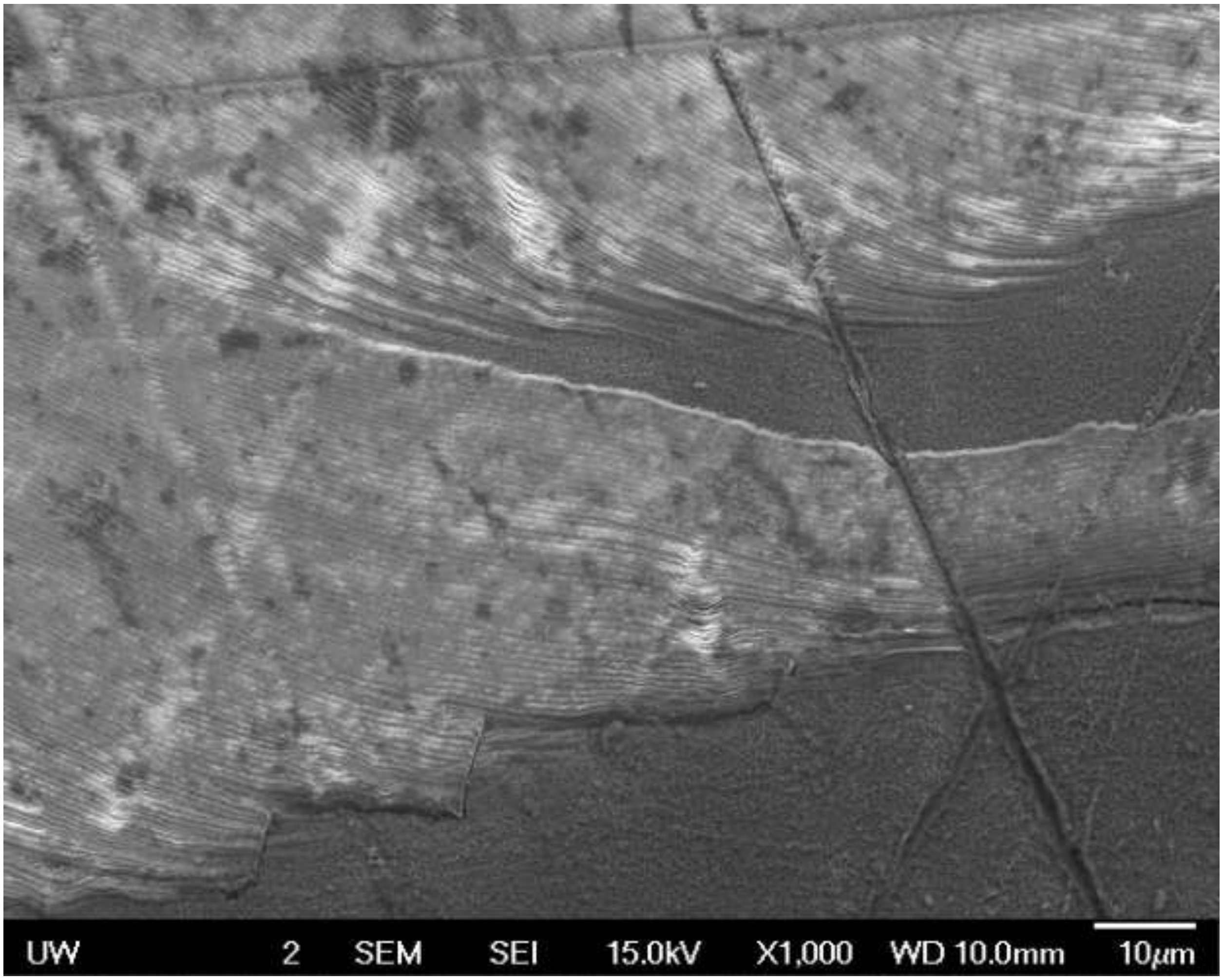

Figure 28. SEM image of OBL LAM A showing detailed view of streaks in the coating at 1000X magnification

Non-planar layers also appeared to more randomly-oriented near the substrate than in other regions of the coating.

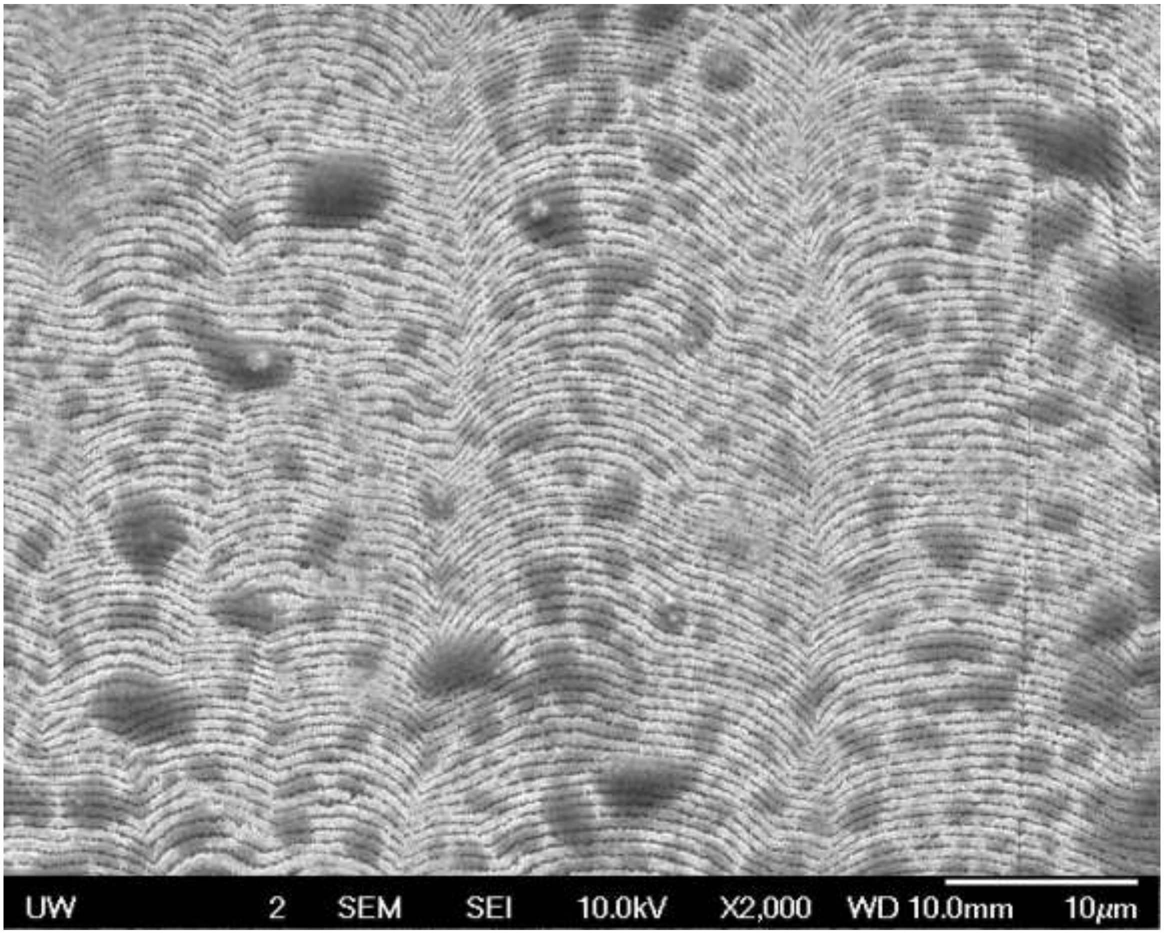

Figure 29. Non-planar layers in SEM image of OBL LAM A at 2,000X magnification near the substrate

Other layer forms of layer inhomogeneity were evident in an overetched sample that had undergone fracture testing (LAM A, Figure 30). It was not entirely unclear from this image alone if the delamination or pitting was an indication of uneven chemical etching or if these morphologies stemmed from electroplating or fracture testing defects that were merely enhanced by etching. Region (1) showed delamination across most of the length of beam. Region (2) showed short-range delamination. Region 3 showed pitting within Region (2).

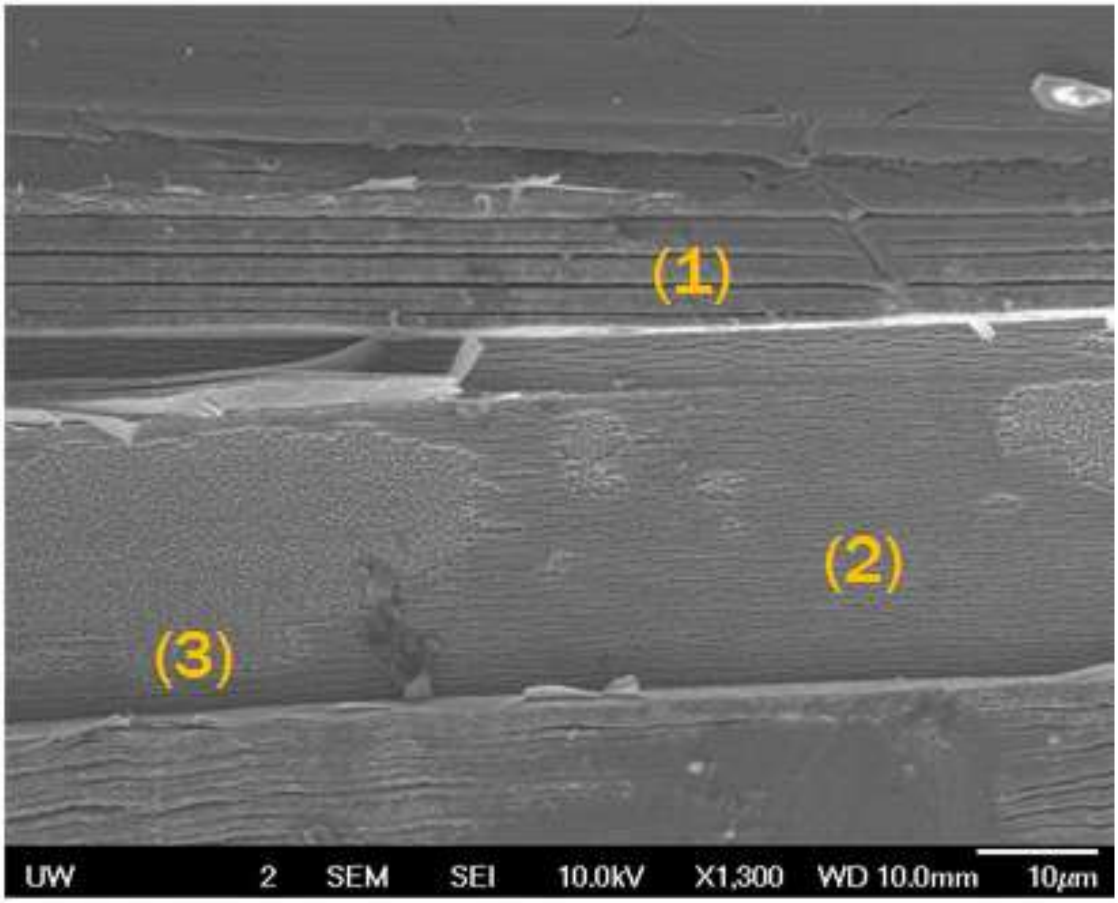

Figure 30. Layer inhomogeneity seen in LAM A under SEM at 1,300X magnification

Examining the area between Regions (2) and (3) further at 10,000X magnification Figure 31, the layers of the nanolaminate became perceptible. Unlike the region with heavy delamination, breaks within the layers were clearly visible as well as short lengths of delamination about two to four μm long. The delamination lines were separated by about 0.5 μm. The layers looked continuous from the higher region through the lower region. Pits in the lower region appeared to have a largely round shape, with sizes varying from layer thickness to as many as perhaps 15 or 20 layers.

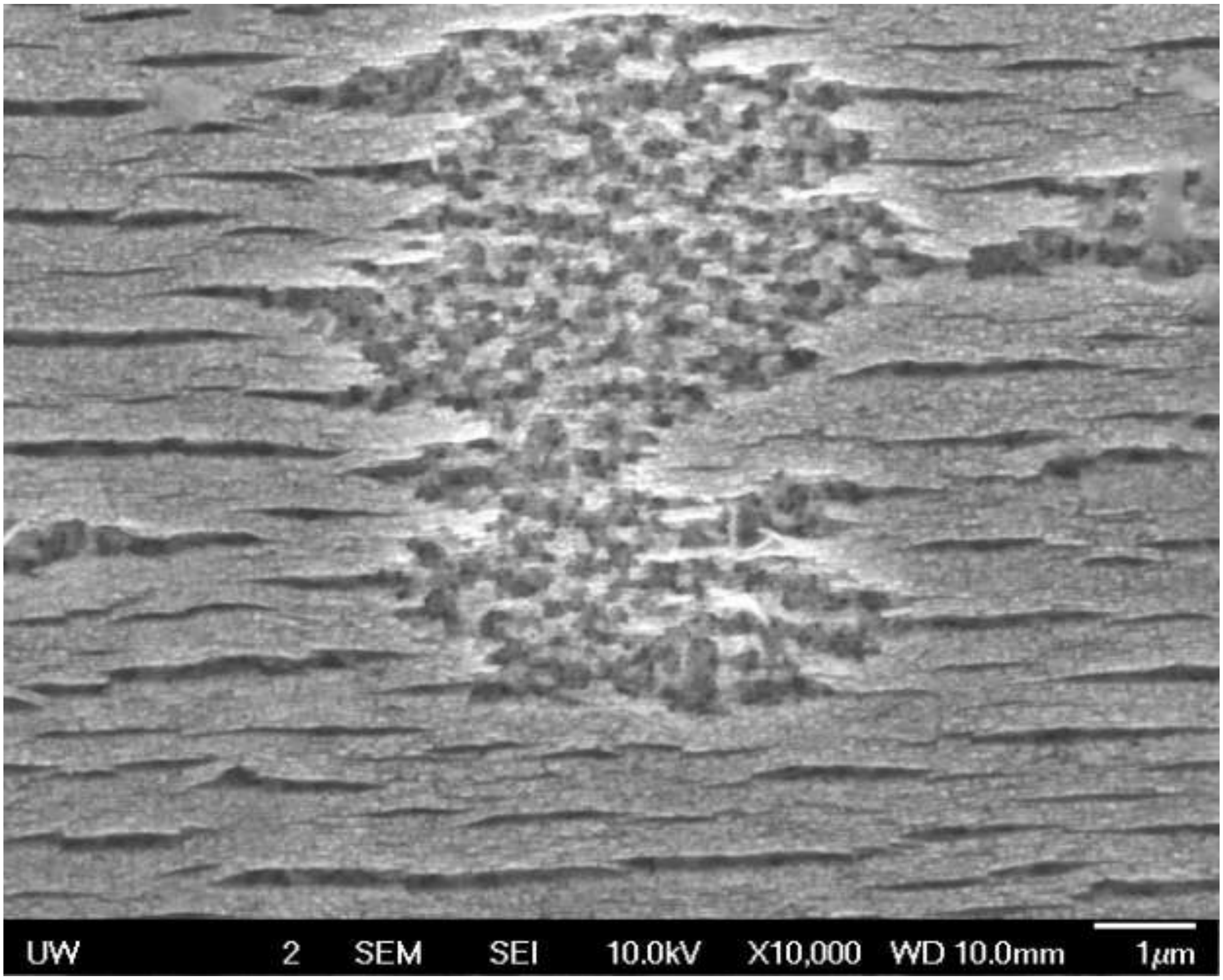

Figure 31. SEM image of LAM A coating showing delamination and regions of pitting at the center of the sample beam at 10,00X magnification

EDS readings were taken of the upper and lower regions to determine the composition around these peculiar formations. EDS revealed that the upper regions are about 55Ni-45Cu in wt% and at%, which is consistent with the composition that was predicted at the beginning of this project and suggests, contrary to the XRD results, that the nanolaminate may not be heavily Ni-rich. The report revealed that the pitted lower region was surprisingly comprised of nearly 90 wt% Cu, similar to the Cu content calculated for the Cu-rich region an unetched sample from overall EDS analysis of the bulk nanolaminate deposit. The SEM image clearly showed nanolamination, so the region was determined not to be a single Cu-rich formation. The increased Cu content did help illuminate why the lower region was so much more severely attacked by the etchant than the upper region.

4.2. Phase Identification from XRD

Figure 32 shows two distinct peaks in the XRD spectrum for the monolithic Ni-rich sample: the first at 2-θ = 44.446°, and the second at 51.799°. The peak locations appeared to be consistent with those of monolithic Cu-Ni deposits from literature, and with the FCC structure of Cu and Ni.

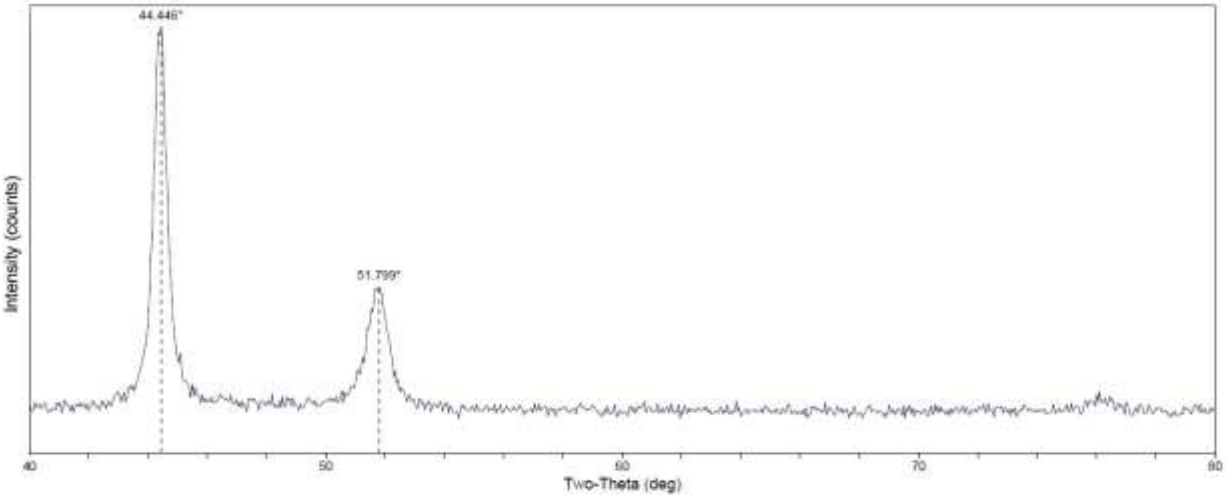

Figure 32. XRD spectrum for monolithic Ni-rich sample

The presence of only two peaks in this range, rather than four distinct peaks corresponding to typical copper and nickel spectra (two for Cu, two for Ni) or the inclusion of several small satellite peaks from peak overlapping, indicated the formation of an interstitial solid solution of the two constituents. This result agrees with the assertion that the sample is a monolithic alloy.

Analysis of the spectrum in Jade showed several possible profile matches, listed in Table 2. “PDF-#” is the Powder Diffraction File Number. Jade’s exact method of calculating figures of merit for a profile’s fit to the sample spectrum is unclear, but the lower the figure of merit, the better the profile’s fit is to the spectrum.

Table 2. Phases identified from XRD spectrum for elemental composition of monolithic Ni-rich sample

Phase	Figure of Merit	PDF-#
Ni - Nickel	8.8	03-065-2865
$(Cu_2Ni_{23})_{0.16}$	10.3	01-077-7710
Cu - Copper	100.8	01-070-3038
(CuNi) - Copper Nickel	100.8	01-071-7832
$(Cu_{19}Ni)_{0.2}$ - Copper Nickel	100.8	01-077-7712
Ni - Nickel	100.8	01-089-7129

Although quantitatively, the figures of merit indicated a best fit with the Ni profile, the $(Cu_2Ni_{23})_{0.16}$ alloy's profile appeared to be a better fit qualitatively when seen overlaid on the sample spectrum in Figure 33. The spiky line is the as-recorded spectrum, the solid outline around it is the profile fit, and the vertical blue lines indicate a match of peak locations to those of the diffraction profile.

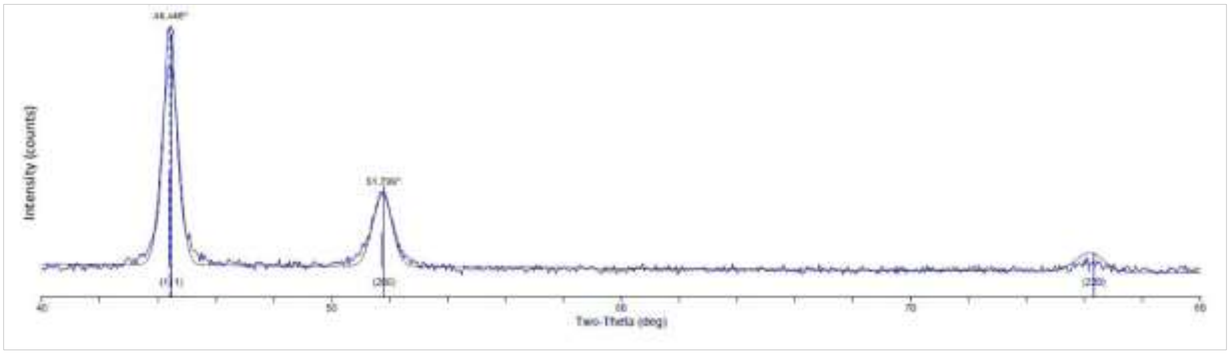

Figure 33. XRD diffraction profile overlay of $(Cu_2Ni_{23})_{0.16}$ on the monolithic Ni-rich sample spectrum

Even with this phase chosen, there was a high residual error of fit value of R = 11.26% (calculated by Jade from weighted background, spectrum, and overlay intensities).

The diffraction spectrum of the nanolaminated Cu-Ni sample shows two distinct peaks in Figure 34 at 44.252° and 51.500°.

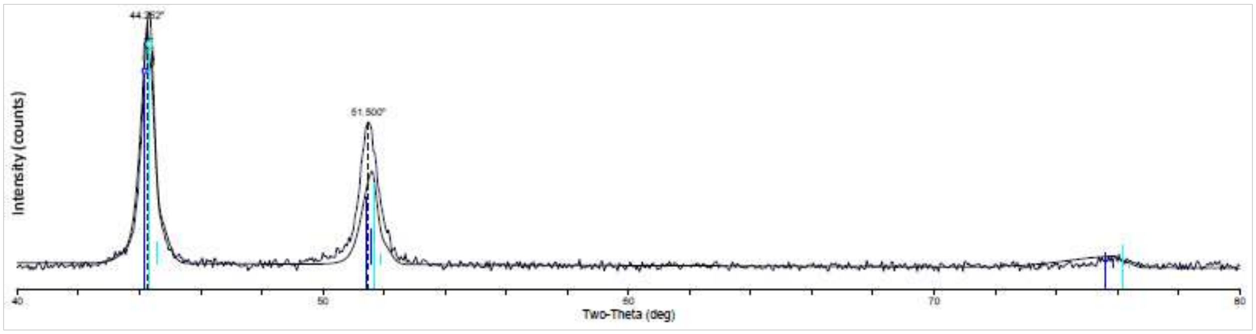

Figure 34. XRD spectrum for nanolaminated sample

The pattern looks nearly identical to that of the monolithic sample – nearly the same peak locations, complete overlap of Cu and Ni peaks to form distinct peaks without satellites – but here the peaks' intensities and widths were slightly different (values listed in Table 4). The ratio of intensities between the first and second peaks of the monolithic sample was 2.56, whereas the ratio in the nanolaminated sample is only 1.58, indicating a compositional difference similar to the one noted in the Baskaran study [16]. In that study, the difference in relative intensity was observed to decrease with increasing Cu content of their samples, as was assumed to be the case here. The lack of separate Cu and Ni peaks suggested a metallic solid solution like the monolithic diffraction spectrum, but such a conclusion would not be accurate because the nanolaminated sample consists of two unique phases, not one. The XRD beam may not be precise enough to distinguish the Cu-rich and Ni-phases from each other.

Jade identified two peak profile matches for potential phases: NiCu (dark blue in spectrum) and Ni (cyan). These both appeared to be a poor qualitative and quantitative fit, with R = 16.1%.

Phase	Figure of Merit	PDF-#
NiCu - Copper Nickel	12.1	03-065-7246
Ni - Nickel	12.5	03-065-2865

Figure 35. Phases identified from XRD spectrum for elemental composition of the nanolaminated sample

4.3. Composition from XRD and EDS

If the monolithic Ni-rich deposit were in fact $(Cu_2Ni_{23})_{0.16}$, then the composition would be 92Ni-8Cu by at% or 91.395Ni-8.605Cu by wt%. The average lattice constant from the quantitative XRD data (Table 3) was 3.5273 Å, which correlates to a Vegard's law composition of 97.445Ni–2.555Cu by at% or 97.239Ni–2.761Cu by wt%.

Table 3. Quantitative XRD data for monolithic Ni-rich sample

Peak #	2-θ (°)	d (Å), lattice plane spacing	Height (electron counts)	Area	Relative Intensity (%)	Full Width Half Max	Crystallite Size (nm)	Miller Indices (h k l)	Lattice Constant (Å)
1	44.446	2.0367	1583	769.6	100.0	0.490	19	1 1 1	3.5276
2	51.799	1.7635	617	322.7	39.0	0.686	13	2 0 0	3.5270

All data from Table 3 was dependent on the actual diffraction pattern, not on the profile overlay.

The peak fit for the nanolaminate sample gave a composition of 78.7Ni-21.3Cu by at% or 67.6Ni-32.4Cu by wt%. The average lattice constant was 3.5442 Å (Table 4), which corresponds to a Vegard's law composition of 78.7Ni-21.3Cu by at% or 77.5Ni-22.5Cu by wt%.

Table 4. Quantitative XRD data for nanolaminated sample

Peak #	2-θ (°)	d (Å), lattice plane spacing	Height (electron counts)	Area	Relative Intensity (%)	Full Width Half Max	Crystallite Size (nm)	Miller Indices (h k l)	Lattice Constant (Å)
1	44.252	2.0452	1327	589.9	100.0	0.436	22.3	1 1 1	3.5423
2	51.500	1.7731	838	467.9	63.1	0.604	15.8	2 0 0	3.5461

Using volume fractions calculated from average nanolaminate layer thicknesses in Table 1 and bulk compositions for the nanolaminate and monolithic Ni-rich deposits calculated from Vegard's Law or the diffraction peak fit, the Cu content of Cu-rich layers was found to be 42.5

wt% and 56.6 wt% Cu, respectively. Both values are far lower than the EDS value of 91.6 wt% Cu. The copper content measured by EDS is thought to be more accurate because the Cu-rich layers etched very easily compared to the Ni-rich ones when the nanolaminate samples were treated with a solution that preferentially attacks Cu. Cu-rich layers were also deposited with plating parameters known to create highly Cu-rich deposits, so the low Cu-content indicated by the XRD values do not seem like reasonable estimates. The discrepancy may be stem from the XRD's inability to distinguish a Cu-rich phase in the nanolaminated sample.

Table 5. Copper content of Cu-rich layers from EDS analysis and calculated from XRD data

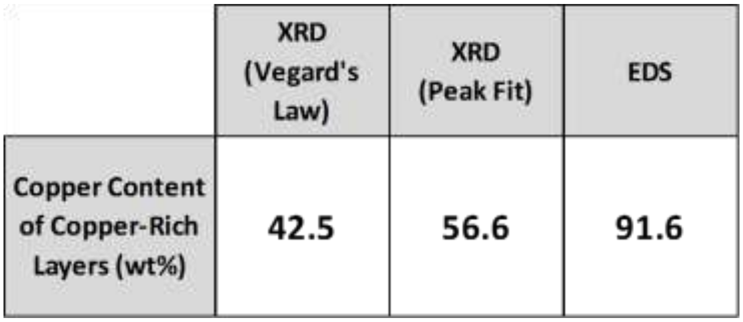

	XRD (Vegard's Law)	XRD (Peak Fit)	EDS
Copper Content of Copper-Rich Layers (wt%)	42.5	56.6	91.6

EDS analysis was also performed on the etched monolithic Ni-rich sample to provide another reference for the actual Cu content of the Ni-rich layers. The composition of the overall MONO coating was found to be 70.91 at% Ni – 29.09 at% Cu, or 69.25 wt% Ni – 30.75 wt% Cu. These differ significantly from the composition values collected from XRD and are closer to the EDS values collected from the unetched samples from previous research. The discrepancy between EDS compositions may be a result of the etching; a strong etchant that preferentially reacts with Ni was used to create definition of microstructures and grains in the alloy. With Ni removed disproportionately with the Cu in the monolithic sample, the Ni content was reduced relative to the Cu content. With this in mind, the 91.6 wt% Cu value again appears to be more plausible than ~40-57 wt% Cu from XRD.

4.4. Grain Sizes from XRD and SEM

Full width half max values of the nanolaminate from XRD were lower than those of the monolithic sample, yielding calculated grain sizes of 22.3 nm and 15.8 nm. The average grain size was therefore 19.1 nm, compared to just 16.0 nm for the monolithic Ni-rich sample. The nanolaminate grain sizes agree with the ~18-50 nm size range from the literature review, but the average grain size of the monolithic sample is much smaller than the 29 nm size reported in literature. It is important to note, though, that the samples in this study were electrodeposited on a rotating disk electrode, whereas the literature studies used static plating baths with agitation from a magnetic stir bar instead. Rotating the substrate during plating increases mass transport of the Cu and Ni ions from the bath to the substrate, increasing the deposition rate as well. With less time to take on a preferred orientation, the grains may be limited to a smaller size. This theory may not be entirely valid, though, because if that were the case, a smaller grain size would have been evident in the nanolaminated sample since speed was increased during deposition of Cu-rich layers. It is more reasonable to assert that because the studies of monolithic samples from literature did not use a grain-refining agent in the plating bath, faceted grains grew rather than the more spherical ones that are common with sodium saccharin addition. With grains approximately the same volume, a faceted or columnar grain would appear to be larger in the XRD spectra than a more uniform or spherical grain. Considering that a spike solution was used in the plating bath in this study to replenish the copper supply, it also seems plausible that the nanolaminated sample was plated either after the addition of a spike solution or after several plating runs in the same bath; decreases in saccharin concentration are known to yield larger grains in Ni-based deposits than with saccharin additions [23]. Sodium saccharin did appear to produce a consistent range of grain sizes in both monolithic and nanolaminated samples in this study. There was a difference of ~30.0% between the largest and smallest detected grain sizes from XRD in each type of deposit.

Under SEM, the coating had a somewhat nodular consistency, with nodes appearing to be about 20-30 nm in diameter in Figure 36. Nodular growths were expected because the presence of saccharin in plating baths has been known to produce spherical grains in electrodeposited nickel thin films [23]. These sizes are not consistent with the grain sizes calculated from XRD, so these structures and the overall texture may merely be relief due to contact with a highly corrosive etchant. Cu-Ni nanolaminates have been known to exhibit grain clustering in a colony-like morphology [2], so the pits may be nodular/spherical grain clusters that were etched out between smooth, polished regions where grains remained. The fact that these round pits are seen close to the substrate and faceted notches were observed far from the substrate may be an indication that the plating bath was becoming depleted of saccharin content. Unfortunately no images could be focused at a magnification greater than 60,000X (notice that the scale bar is only 100 nm long), so no grains were distinguishable. The coating appeared to be uniformly textured, similar to those observed by Pellicer *et al* [1].

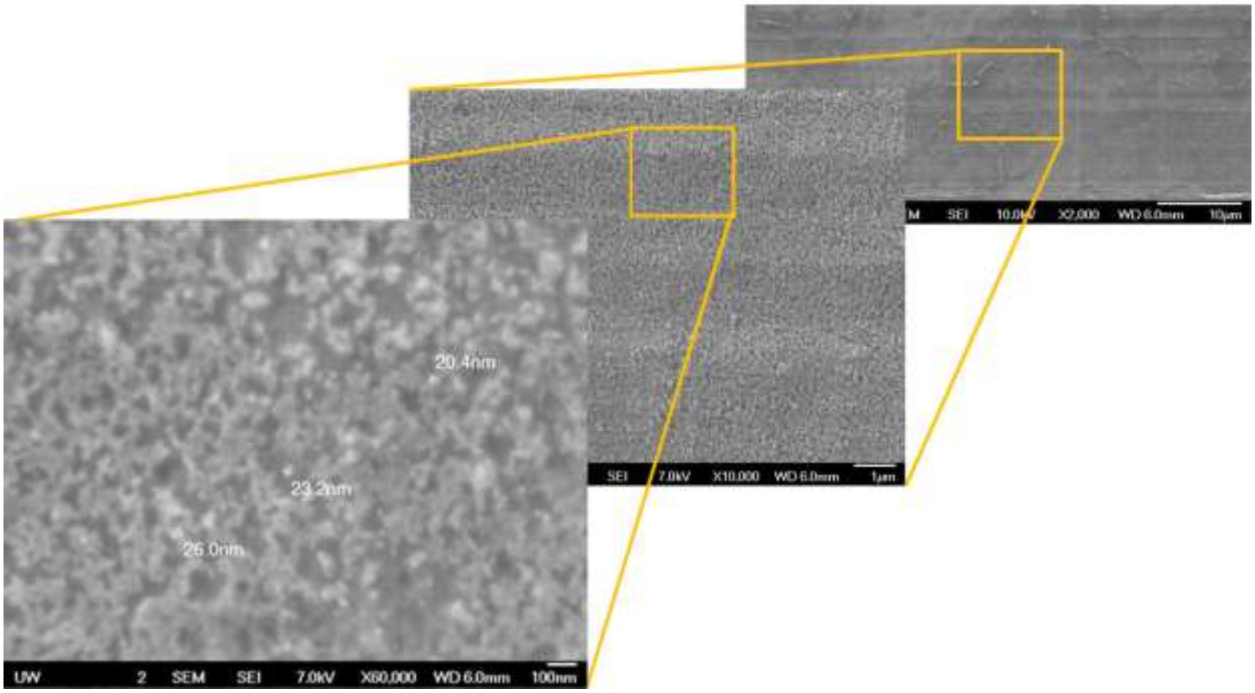

Figure 36. SEM image of monolithic Ni-rich coating showing spongy-like texture of round protrusions and pits at 60,000x magnification

A similar texture and more spherical pits were seen in the Ni-rich top coat of the nanolaminated deposit after the Cu etching.

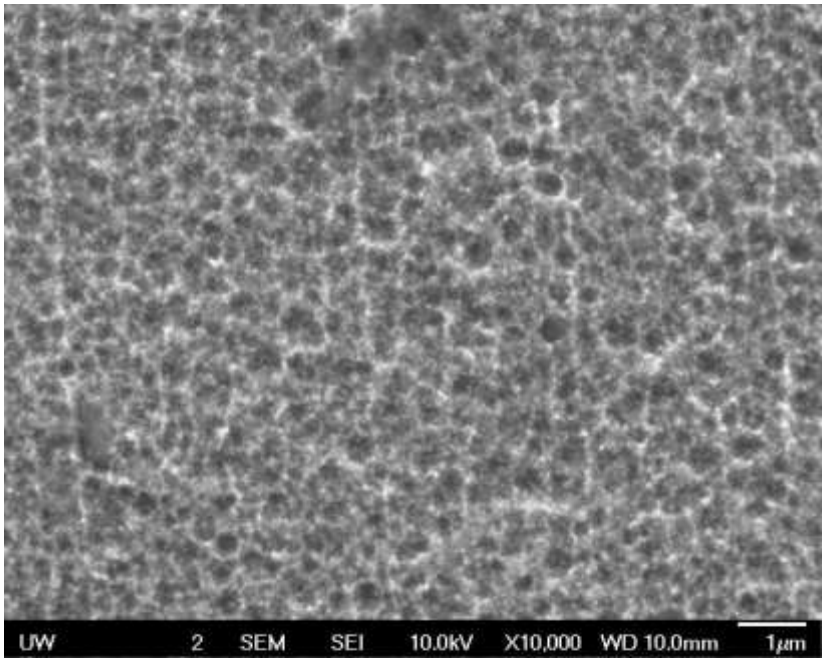

Figure 37. Spherical pits and uniform texture observed in Ni-rich top coat of OBL LAM A under SEM at 10,000X magnification

This pattern was also evident in heavily delaminated areas of LAM A after overetching Cu-rich regions. The pit sizes ranged from 33.8-78.8 nm.

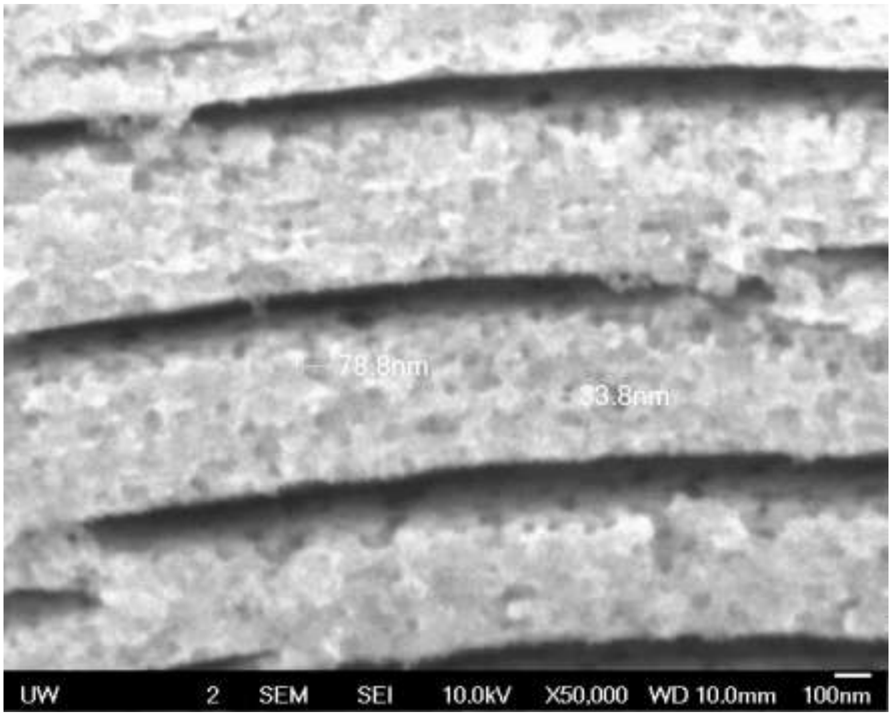

Figure 38. SEM image of LAM A near substrate showing round pits at 50,000X magnification

Pit sizes ranged between ~40 and 65 nm in OBL LAM A in the sides of the Ni-rich layers where Cu-rich layers had been etched out. The spherical shape of the recessed pits again supports the notion that the grains may have formed large round grain colonies from saccharin addition to the bath.

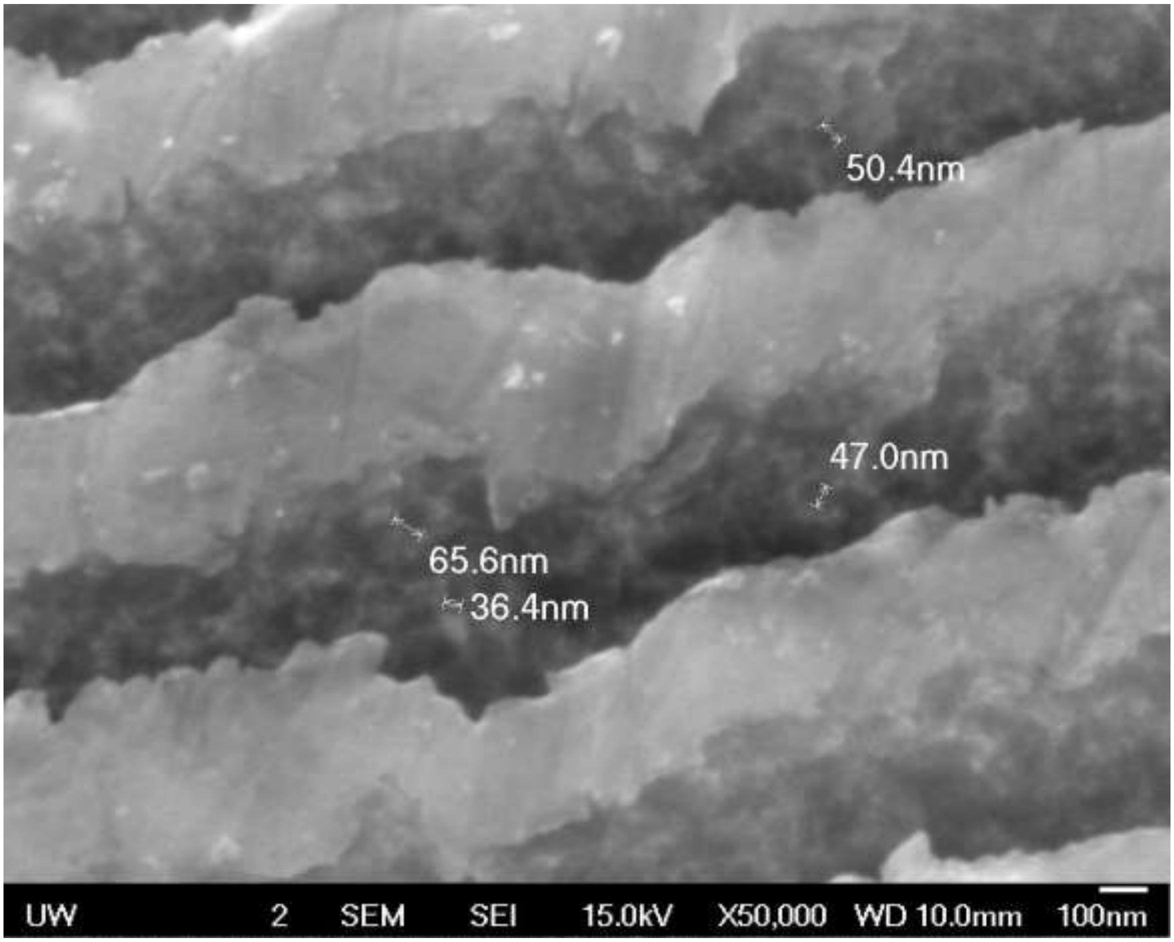

Figure 39. SEM image of round pits between etched layers of OBL LAM A

5. Conclusions

Significant contributions have been made to the current study of structure-processing-property relationships of the Cu-Ni nanolaminate system. Nanolaminated samples exhibited a non-uniform microstructure, though possible grain structure in the form of grain colonies was successfully observed despite the lack of SEM capability to resolve the ~20 nm grains. Laminate structure was also characterized, with regions of planar and non-planar layers evident throughout the nanolaminate deposit. Non-planar layers were most prevalent near the substrate and adjacent to large Cu-rich streaks seen in the coating. These and other defects indicate that the increase in rotation speed during Cu-rich deposition is detrimental to the homogeneity of layer formation. Phase compositions of the Cu-rich and Ni-rich layers were inconclusive because of disparity between XRD and EDS data, though the EDS estimates of 91.6 wt% Cu in Cu-rich and 19.0 wt% Cu in Ni-rich is thought to be more accurate since the XRD had difficulty identifying distinct phases within the nanolaminate and ease of etching suggested high copper content within Cu-rich layers. These conclusions provide a better understanding of the fracture behavior of Cu-Ni nanolaminates as it relates to processing (unique to rotating disk electrode deposition) and structural properties. They provide a guide for future processing and characterization of future electrodeposited Cu-Ni nanolaminate samples.

6. Future Work

Refinement of the etching process is recommended to yield more consistent layer definition and potential grain structure within laminates. Difficulty with phase identification in XRD might also be alleviated with the use of equipment better suited for nanocharacterization of nanolaminate phases in solid samples rather than merely powdered samples (i.e. diffraction peak profiles for solid samples if XRD).

TEM imaging may also be better suited to resolve the nanocrystalline grains, though it would not provide valuable information until more uniform nanolaminate deposits are produced. AFM imaging may provide valuable structural information as well.

References

[1] E. Pellicer, A. Varea, S. Pane, K. M. Sivaraman, B. J. Nelson, S. Surinach, M. D. Baro and J. Sort, "A comparison between fine-grained and nanocrystalline electrodeposited Cu-Ni films. Insights on mechanical and corrosion performance," *Surf Coat Tech,* vol. 205, pp. 5285-5293, 2011.

[2] M. Agarwal, V. Kumar, S. Malladi, R. Balasubramaniam and K. Balani, "Effect of current density on the pulsed co-electrodeposition of nanocrystalline nickel-copper alloys," *JOM,* vol. 62, no. 6, pp. 88-92, 2010.

[3] V. F. Lins, E. S. Cecconello and T. Matencio, "Effect of the Current Density on Morphology, Porosity, and Tribological Properties of Electrodeposited Nickel on Copper," *J. Mater. Eng. Perform.,* vol. 17, no. 5, pp. 741-745, 2007.

[4] Y. Kaneko, Y. Mizuta, Y. Nishijima and S. Hashimoto, "Vickers hardness and deformation of Ni/Cu nano-multilayers electrodeposited on copper substrates," *J Mat Sci,* vol. 40, pp. 3231-3236, 2005.

[5] N. Rajasekaran and S. Mohan, "Structure, microstructure and corrosion properties of brush-plated Cu-Ni alloy," *J Appl Electrochem,* vol. 39, pp. 1911-1916, 2009.

[6] G. S. Was and T. Foecke, "Deformation and fracture in microlaminates," *Thin Solid Films,* vol. 286, pp. 1-31, 1996.

[7] S. K. Ghosh, A. K. Grover, G. K. Dey and M. K. Totlani, "Nanocrystalline Ni-Cu alloy plating by pulse electrolysis," *Surf Coat Tech,* vol. 126, pp. 48-63, 2000.

[8] Modumetal, LLC., "Corrosion," [Online]. Available: http://modumetal.com/corrosion.php. [Accessed 28 November 2012].

[9] G. S. Rohrer, Models for predicting phase stability, Cambridge: Cambridge University, 2001, pp. 425-426.

[10] S. K. Ghosh, A. K. Grover, G. K. Dey, U. D. Kulkarni, R. O. Dusane, A. K. Suri and S. Banerjee, "Structural characterization of electrodeposited nanophase Ni-Cu alloys," *J Mater Res,* vol. 21, no. 1, pp. 45-61, 2006.

[11] M. de los A. Cangiano, M. W. Ojeda, A. C. Carreras, J. A. Gonzalez and M. del C. Ruiz, "A study of the composition and microstructure of nanodispersed Cu-Ni alloys obtained by different routes from copper and nickel oxides," *Mater Charact,* vol. 61, pp. 1135-1146, 2010.

[12] S. K. Ghosh, G. K. Dey, R. O. Dusane and A. K. Grover, "Improved pitting corrosion behaviour of electrodeposited nanocrystalline Ni-Cu alloys in 3.0wt.% NaCl solution," *J Alloy Compd,* vol. 426, pp. 235-243, 2006.

[13] G. Abadias, A. Michel, C. Tromas, C. Jaouen and S. N. Dub, "Stress, interfacial effects and mechanical properties of nanoscale multilayered coatings," *Surf Coat Tech,* vol. 202, pp. 844-853, 2007.

[14] E. Pellicer, A. Varea, K. M. Sivaraman, S. Pane, S. Surinach, M. D. Baro, J. Nogues, B. J. Nelson and J. Sort, "Grain boundary segregation and interdiffusion effects in the nickel-copper alloys: an effective means to improve the thermal stability of nanocrystalline nickel," *ACS Appl. Mater. Interfaces,* vol. 3, pp. 2265-2274, 2011.

[15] B. D. Cullity and S. R. Stock, Crystallite Size, Upper Saddle River: Prentice Hall, 2001, pp. 167-171.

[16] I. Baskaran, T. S. Narayanan and A. Stephen, "Pulsed electrodeposition of nanocrystalline Cu-Ni alloy films and evaluation of their characteristic properties," *Mater Lett,* vol. 60, pp. 1990-1995, 2006.

[17] B. D. Cullity and S. R. Stock, "Crystallite Size," in *Elements of X-Ray Diffraction*, Upper Saddle River, Prentice Hall, 2001, pp. 167-171.

[18] N. Rajasekaran and S. Mohan, "Preparation, corrosion and structural properties of Cu-Ni multilayers from sulphate/citrate bath," *Corros Sci,* vol. 51, pp. 2139-2143, 2009.

[19] L. Bonou, Y. Massiani and J. Crousier, "Electrodeposition and corrosion behavior of copper-nickel alloys," *Brit. Corros. J.,* vol. 29, no. 3, pp. 201-205, 1994.

[20] F. Ebrahimi and A. J. Liscano, "Microstructure/mechanical properties relationship in electrodeposited Ni/Cu nanolaminates," *Mat Sci Eng A-Struct,* vol. 301, pp. 23-34, 2001.

[21] NDT Resource Center, "X-Ray Generators," [Online]. Available: http://www.ndt-ed.org/EducationResources/CommunityCollege/Radiography/EquipmentMaterials/xrayGenerators.htm. [Accessed 1 June 2012].

[22] JEOL, "JSM-7000F Optimized Specimen Chamber Geometry," 2006-2012. [Online]. Available: http://www.jeol.com/RESOURCES/ProductPresentations/JSM7000FOptimizedSpecimenChamberGeometry/tabid/355/Default.aspx. [Accessed 1 June 2012].

[23] A. C. Mishra, A. K. Thakur and V. Srinivas, "Effect of deposition parameters on microstructure of electrodeposited nickel thin films," *J. Mater. Sci,* vol. 44, pp. 3520-3527, 2009.

[24] C. Bonhote and D. Landolt, "Microstructure of Ni-Cu multilayers electrodeposited from citrate electrolyte," *Electrochimica Acta,* vol. 42, no. 15, pp. 2407-2417, 1997.

[25] ASM International, "Metallurgy and Microstructures," *ASM Handbook Volume 9,* p. 778, 2004.

[26] W. F. Gale and T. C. Totemeir, Smitells Metals Reference Book, 8th ed., Elsevier

Butterworth-Heinemann, 2004, p. 995.